ACS OMEGA

http://pubs.acs.org/journal/acsodf

Article

Fe Nanoparticle Size Control of the Fe-MOF-Derived Catalyst Using a Solvothermal Method: Effect on FTS Activity and Olefin Production

Ahmed E. Rashed,* Alhassan Nasser, Marwa F. Elkady, Yoshihisa Matsushita, and Ahmed Abd El-Moneim*

Cite This: *ACS Omega* 2022, 7, 8403−8419

Read Online

ACCESS | Metrics & More | Article Recommendations | Supporting Information

ABSTRACT: The design of a highly active Fe-supported catalyst with the optimum particle and pore size, dispersion, loading, and stability is essential for obtaining the desired product selectivity. This study employed a solvothermal method to prepare two Fe-MIL-88B metal−organic framework (MOF)-derived catalysts using triethylamine (TEA) or NaOH as deprotonation catalysts. The catalysts were analyzed using X-ray diffraction, N_2-physisorption, Fourier transform infrared spectroscopy, scanning electron microscopy, transmission electron microscopy, H_2 temperature-programed reduction, and thermogravimetric analysis and were evaluated for the Fischer−Tropsch synthesis performance. It was evident that the catalyst preparation in the presence of TEA produces a higher MOF yield and smaller crystal size than those produced using NaOH. The pyrolysis of MOFs yielded catalysts with different Fe particle sizes of 6 and 35 nm for the preparation in the presence of TEA and NaOH, respectively. Also, both types of catalysts exhibited a high Fe loading (50%) and good stability after 100 h reaction time. The smaller particle size TEA catalyst showed higher activity and higher olefin yield, with 94% CO conversion and a higher olefin yield of 24% at a lower reaction temperature of 280 °C and 20 bar at $H_2/CO = 1$. Moreover, the smaller particle size TEA catalyst exhibited higher Fe time yield and CH_4 selectivity but with lower chain growth probability (α) and C_{5+} selectivity.

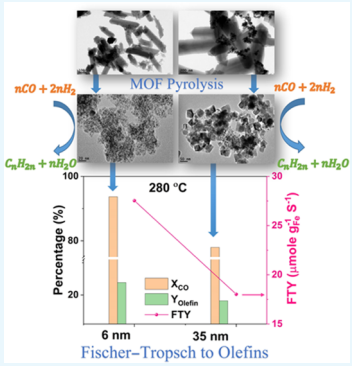

1. INTRODUCTION

The production of olefins, exceptionally light olefins, is one of the most critical and energy-intensive processes in the petrochemical industry.[1,2] Several methods have been developed to produce olefins which include mainly steam cracking of hydrocarbons[3] and other new technologies such as the oxidative coupling of methane,[4] the methanol-to-olefins process,[5] and the Fischer−Tropsch-to-olefins process.[6] The Fischer−Tropsch synthesis (FTS) technology is an essential route to olefins and other petrochemicals such as diesel, jet fuels, gasoline, alcohols, and lubricating oils.[7,8] The most important FT catalysts are Fe, Co, and Ni. Ni is not favored in FT synthesis due to its very high methane selectivity and short lifetime.[9] Co is more resistant to the water−gas shift reaction and deactivation than Fe catalysts.[10] However, it is more expensive and limited to the low-temperature FT (LTFT) conditions due to its high methane selectivity at the high-temperature FT (HTFT) range.[10]

Fe is a very versatile and active FT catalyst. It can work in both LTFT and HTFT conditions. At HTFT conditions, it is selective for light olefins and alkanes.[11] However, this selectivity can be significantly improved by using promoters and carbon supports, as discussed later.[12−14] Other FT catalysts, such as Ru and Rh, show exceptionally high FT activity in both temperature ranges. However, there is a big limitation in their use as FT catalysts due to their high cost.[15]

FT promoters are elements that can promote the FT performance and desired product selectivity of the active catalysts without catalyzing the reaction itself.[15] Common FT promoters include alkali earth metals, Mg, Ca, Mn, and S.[16−18]

Catalysts, in general, are either free-standing or supported catalysts. Catalysts with support, such as metal oxides and mesoporous materials,[19,20] have the advantages of better catalyst dispersion on the support surface, smaller catalyst particle size, and higher active site density and active surface area.[21] It is crucial to consider the metal−support interaction (MSI) when using the support. For example, it is known with SiO_2 supports that Fe catalysts form iron silicates when exposed to prolonged FTS service time. The strong MSI formed between SiO_2 and the active catalyst causes deactivation of the catalyst.[21] Other supports have a very weak MSI, allowing for the gradual migration, agglomeration, and sintering of the catalyst particles, lowering the FT activity. It is thus essential to design the catalyst's support to have a

Received: October 22, 2021
Accepted: January 25, 2022
Published: February 28, 2022

moderate MSI to ensure a good, long, and stable catalyst lifetime and performance.

In view of the concerns mentioned above, a suitable catalyst is required to balance between high activity, high stability, high dispersion of active metal, high metal loading, high diffusion of gas feed, weak MSI, abundance, and low cost. Mesoporous materials have the advantages of large surface area, improved accessibility, and high dispersion of active sites.[22] Carbonaceous materials, such as graphene,[16,23,24] carbon nanotubes,[25] and metal−organic framework (MOF)-derived supports,[26] are vital mesoporous materials due to the electronic handover between carbon and the active metal, moderate MSI, chemical stability, modifiable surface area, and improved reducibility of the active metal.[18,21]

MOFs are a new group of materials that have an extensive surface area with a tunable porous structure. They have a unique crystalline structure with a uniform micro- or mesoporous framework composed of organic linkers and metal clusters.[27] Unlike traditionally supported catalysts, MOFs do not involve postsynthetic techniques such as wet impregnation, which may lead to a partial loss of mesoporosity and less control on the dispersion of active sites.[18,22] Alternatively, after pyrolysis of parent MOFs, superior metal dispersion inside the carbon matrix of the MOF-derived catalyst is acquired, which is attributed to the atomic-level distribution of the metal in its crystalline structures. As mentioned before, high metal loading is necessary for high activity but is achieved at the expense of lower dispersion and lower surface area due to the larger metal particles accompanied with higher concentration. This puts a threshold of 30 wt % of metal loading and results in a loss of active metal surface area.[21] MOF-derived catalysts can overcome this limitation and obtain catalysts of high metal loading and narrow distribution of small metal nanoparticles.[28]

Compared to conventional inorganic porous solids, MOFs have relatively lower thermal and chemical stability.[29] It is considered as the main limitation for MOF utilization in catalytic reactions. Despite the robustness of several MOF-based catalysts, it is hard to expect its stability without experimental analysis under a range of operating conditions. In addition, the high cost of certain organic linkers precursors should be considered and assessed based on the obtained high catalytic performance and product yield.

Recently, MOFs proved to be a successful precursor for preparing an active FT catalyst with well-dispersed iron nanoparticles in a mesoporous carbon support.[30−33] Santos *et al.*[33] were the first to use an MOF-mediated synthesis strategy to prepare a series of Fe-derived MOF catalysts by direct pyrolysis of Fe-BTC with high Fe loading and dispersion where their catalytic activity outweighs that of known industrial catalysts with high light olefins selectivity. Later, Santos and his group used the same strategy to investigate the effect of different pyrolysis temperatures[34] and to study a series of catalysts prepared from different MOFs.[35] They concluded that the structure and composition of the parent MOFs strongly affect the succeeding MOF-derived catalyst in terms of the catalytic activity and product distribution. In addition, An *et al.*[36] prepared core−shell Fe_3O_4@Fe_5C_2 catalysts by pyrolysis of Fe-MIL-88B and ended with a higher Fe time yield (FTY) than that of other reported Fe-MOF-derived catalysts to date. The work of Santos' group and An's group paved the way for further investigation of iron-based MOFs from different perspectives.[18,26,37−40] However, the study of iron-based MOFs is still limited and needs to be further explored.

Several studies proposed that the textural properties of the support and the pore size and particle size of the active metal considerably impact catalytic activity and olefin selectivity.[41,42] However, the pore size effect appears to be overlapping with the particle size effect.[41,43] The effect of metal particle size on FTS performance has been generally studied on Fe, Co, and Ru catalysts.[42,44]

The work of Iglesia[45] and Bezemer[46] groups on cobalt catalysts established an optimum range of 6−8 nm for Co particle size, above which catalytic performance was independent of particle size. They showed a decrease in activity and an increase in methane selectivity (S_{CH_4}) below this range. In contrast, Jung[47] and Jones[48] groups indicated a decrease in both activity and S_{CH_4} for iron catalysts with particle sizes below 9 nm. However, both groups reported diverging olefin/paraffin (O/P) ratio values for smaller particles. Additionally, the work of Jung[47] and Jones[48] is in partial agreement with the subsequent work accomplished by van Steen's group[49,50] with the optimum particle size = 7−9 nm and that of Park *et al.*[51] with the optimum particle size = 6.2 nm. The later groups indicated an activity decline below the particle size threshold but with a decrease in S_{CH_4}.

Further work on promoted and unpromoted Fe catalysts for HTFT synthesis was performed by the de Jong group,[52−54] Gu *et al.*,[12] and Liu *et al.*,[55] who concluded that the catalytic activity of the unpromoted catalyst reaches its maximum at a threshold particle size of about 6 nm. Above this threshold, activity remained constant, which is consistent with the work of van Steen's group[49,50] and Park *et al.*[51] on promoter-free Fe-based catalysts. In addition, the size of iron nanoparticles did not significantly affect the olefin selectivity and O/P ratio for unpromoted catalysts. In contrast, the work of the de Jong group[52−54] on Na- and S-promoted catalysts, Gu *et al.*[12] on Bi- and Pb-promoted catalysts, and Liu *et al.*[55] on Mn-promoted catalysts showed that the light olefin selectivity ($S_{C_2-C_4^=}$) and O/P ratio tend to correlate with particle size above the 6 nm threshold. Moreover, Sun *et al.*[56] and Lablokov *et al.*[57] reported contrasting results that are also partially consistent with the work mentioned above.

According to the above debatable results from studies on the iron particle size effect, several factors with complex interaction could explain the contradicting correlation of particle size with FTS performance. The use of various support materials, Fe loadings, promoters, reducibilities, porous structures, and operating conditions, along with the probability of olefin readsorption and secondary reactions in a confined space, makes it difficult to demonstrate the sole effect of particle size on activity and product distribution.[44,55,58] Thus, further investigation is needed to achieve consistency of the iron particle size effect, primarily for Fe-MOF derived catalysts with a limited number of studies and coinciding factors that may mask the effect of particle size.[33,34] Therefore, the novelty of this work is to focus on the sole effect of iron particle size on catalytic performance while alleviating the effect of other overlapping factors.

The catalyst preparation method significantly influences the structural properties of the prepared catalysts and, hence, their catalytic activity.[59] This work evaluates the FTS performance of two catalysts derived from the Fe-MIL-88B MOF, which is commonly prepared by the solvothermal reaction of the 1,4-

https://doi.org/10.1021/acsomega.1c05927
ACS Omega 2022, 7, 8403−8419

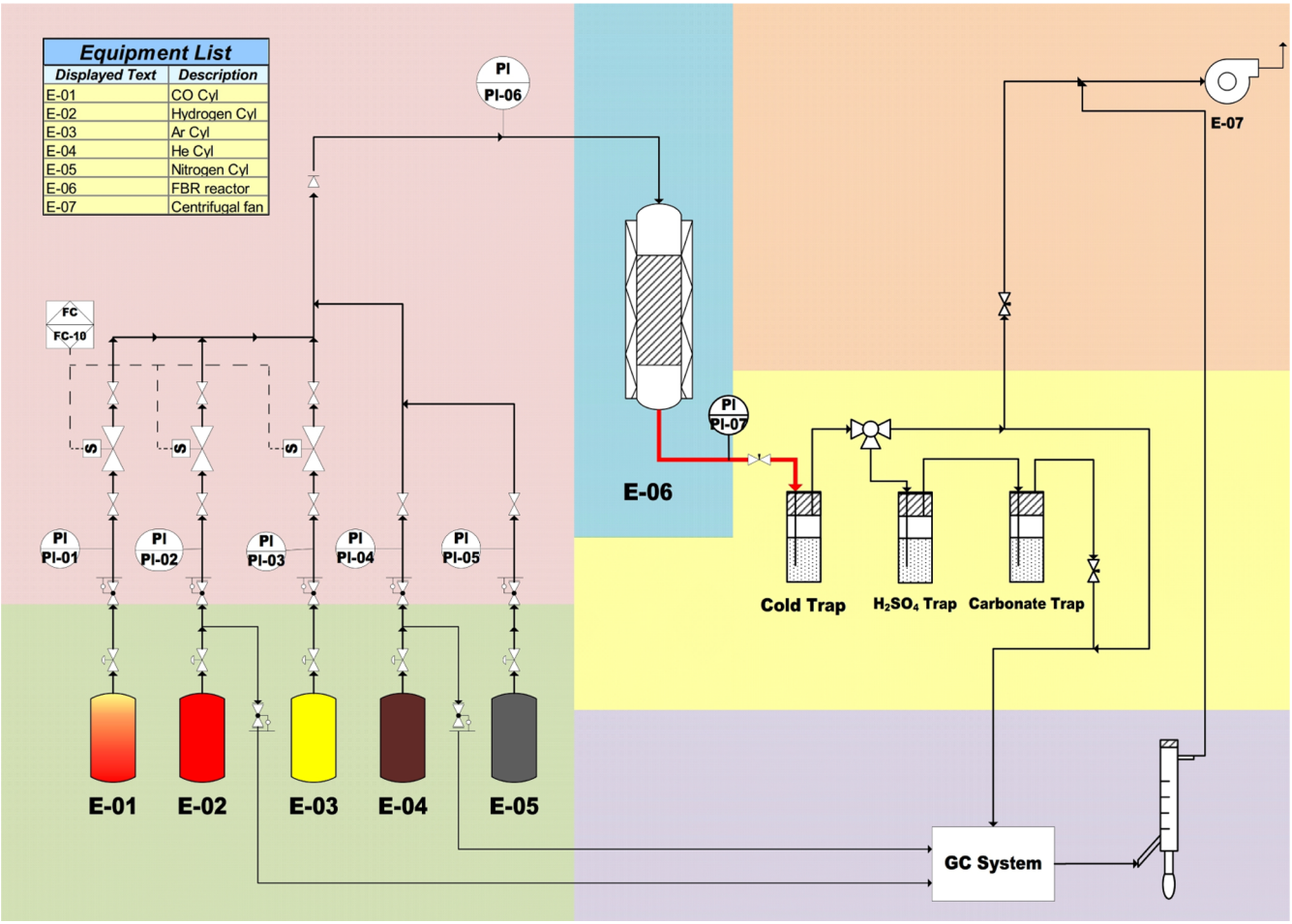

Figure 1. Schematic illustration of the FTS unit. Reprinted with permission from [Nasser, A. L. H.; El-Naggar, H.; El-Bery, H.; Basha, I.; Abdelmoneim, *RSC Adv.*, **2019**, *9*, 10937].[14]

benzezedicarboxylate (BDC) linker (terephthalic acid or H_2BDC) and Fe precursor in a dimethylformamide (DMF) solvent in the presence of NaOH as a catalyst for H_2BDC deprotonation.[36,60] The use of DMF as a solvent is preferred as H_2BDC is water-insoluble. However, the H_2BDC reaction with NaOH gives a DMF-insoluble Na_2BDC salt. This procedure is likely to cause blockage of the porous structure and large crystal formation, which makes water a preferred choice of solvent when using NaOH.[61] Alternatively, when triethylamine (TEA) is used as a catalyst, it generates a DMF-soluble carboxylic form that can easily be complexed with metal ions and rapidly form MOFs with a highly porous structure. This procedure is commonly used to prepare small nanosized crystals of BDC-based MOFs at lower temperatures, especially at room temperature.[62]

Utilizing both NaOH and TEA as catalysts for H_2BDC deprotonation is believed to influence the structural properties of Fe-MIL-88B MOFs and is targeted to obtain Fe-MOF-derived catalysts with different Fe particle sizes. Textural properties, including particle size, are considered to be relatively preserved after the pyrolysis of parent MOFs. This work aims to address the single effect of iron particle size for the two prepared unpromoted Fe-MOF-derived catalysts and to maximize the catalytic activity and olefin yield by optimizing the operating conditions while other interrelating parameters such as Fe loading, pore size, and support were kept relatively similar.

2. EXPERIMENTAL SECTION

2.1. Fe-MIL-88B MOF Synthesis. Two Fe-MIL-88B MOFs (Fe-MIL-88B/S and Fe-MIL-88B/T) were synthesized by using a solvothermal method in the presence of different catalysts for terephthalic acid deprotonation (NaOH for Fe-MIL-88B/S MOF or TEA for Fe-MIL-88B/T MOF) according to Horcajada *et al.*[63] and as in our previous work[64] with minor modifications.

2.1.1. General Procedure for Preparation of the Two Fe-MIL-88B MOFs. 1 mmol (232 mg) terephthalic acid, 0.8 mL of NaOH [or 3.58 mmol (500 μL) of TEA], and 1 mmol (808 mg) $Fe(NO_3)_3$ were mixed in 10 mL of DMF at room temperature. Then, each mixture was transferred to a 60 mL autoclave at 100 °C for 12 h. The reddish-brown precipitate was centrifuged, and washed with DMF, deionized water, and ethanol. Finally, the product was activated by drying in a vacuum oven at 60 °C overnight.

2.2. Preparation of the Fe-MOF-Derived Catalyst Using a Pyrolysis Technique. Dried MOFs were ground and pyrolyzed under the flow of nitrogen for 4 h at 500 °C. The temperature was maintained at 60 °C for 1 h then increased to 500 °C (5 °C min^{-1}). Finally, the produced catalysts (Fe-MIL-88B-S/C and Fe-MIL-88B-T/C) were passivated under a slow flow of 1% O_2/Ar to prevent burning when exposed to air.

https://doi.org/10.1021/acsomega.1c05927
ACS Omega 2022, 7, 8403−8419

2.3. Materials Characterization for Identification of the Physiochemical Properties. Thermogravimetric analysis (TGA) under air was performed to evaluate iron loadings using a TGA-50, Shimadzu instrument with a temperature scan from 25 to 800 °C (10 °C min^{-1}). Iron loadings were calculated using equations in ref 38, assuming complete oxidation toward Fe_2O_3. Fourier transform infrared spectroscopy (FTIR) spectra were produced using a Bruker Vertex 70 to explore the change in chemical properties pre-and post-pyrolysis. X-ray diffraction (XRD) patterns were plotted using a Shimadzu XRD-6100 with Cu Kα radiation at 10−80° to detect phases. To examine the morphological structure, particle size distribution (PSD), and dispersion, scanning electron microscopy (SEM) and transmission electron microscopy energy-dispersive X-ray spectroscopy (TEM−EDX) images were obtained using JEOL JSM-6010LV and JEOL JEM-2100F microscopes, respectively.

N_2 adsorption isotherms were determined using a BEL Japan (BELSORP II mini) and analyzed using the Brunauer−Emmett−Teller (BET) and Barrett−Joyner−Halenda (BJH) *t*-plot methods to calculate BET surface area, mean pore diameter, and total pore volume. The as-prepared and pyrolyzed MOFs were degassed at 150 °C overnight before measurements. H_2 temperature-programed reduction (H_2-TPR) data were recorded using a BELCAT II catalyst analyzer, equipped with a thermal conductivity detector (TCD) to determine the steps and degree of reduction. Results were recorded from room temperature to 900 °C at a heating rate of 10 °C min^{-1} under 30 mL min^{-1} stream of 5.2 vol % H_2/Ar.

2.4. Catalyst Performance Evaluation. In all FTS runs, 0.5 g of the catalyst was diluted by an equivalent volume of SiC and loaded into a fixed bed reactor, the layout of which is shown in Figure 1. Due to the importance of resistance to chemical corrosion,[65,66] the reactor material was chosen to be stainless steel (316 grade) for its reasonable cost and higher corrosion resistance than that of alternative alloys. Catalyst reduction was conducted at 400 °C (10 °C min^{-1}) under 50 mL min^{-1} flow of H_2 for 4 h, and then, the reactor was cooled down to 180 °C. Next, the reactor was heated to the desired reaction temperature, that is, when syngas was introduced at 300 psi, $H_2/CO = 1$, and a gas hour space velocity (GHSV) of 4200 mL g_{cat}^{-1} h^{-1}. The cold trap was filled with 20 mL of deionized water and 2 g of *n*-octane at 3 °C.

The composition of the permanent gases (CO, CH_4, and CO_2) was monitored using a gas chromatography (GC)/TCD system (Shimadzu-GC-2014) with a 3 m ShinCarbon Restek column. Their molar concentrations were calculated using external standards of the three gases. In the GC/TCD system, the temperature of the injection ports was set at 100 °C, that of the column at 120 °C, and that of the TCD detector at 180 °C, while the He carrier gas flow rate was 20 mL min^{-1}.

The light hydrocarbon fraction (C_1−C_6) was measured in a GC/flame ionization detection (FID) system (Shimadzu-GC-2014) equipped with a Rt-alumina BOND/Na_2SO_4 column (30 m, 0.32 mm ID, 5 μm film). The GC/FID system was calibrated using external secondary standard gas (C_1−C_6) obtained from a Petroleum company. The FID oven was kept at 40 °C for 6 min and then increased to 100 °C (15 °C min^{-1}) for 37 min. The linear velocity of the carrier gas (He) was 40 cm s^{-1} while samples were injected at a split ratio of 150.

The liquid fraction was mixed with *n*-dodecane as an internal standard and then was analyzed using direct injection on a MXT-1 Restek column (60 m, 0.53 mm ID, 5 μm film)—GC system (SRI-8610C-GC). The oven temperature for the column was kept at 35 °C for 3 min, followed by ramping up to 240 °C (5 °C min^{-1}), next increased to 300 °C (10 °C min^{-1}), and finally maintained at this value for 60 min. The carrier gas (He) was supplied at a flow rate of 5 mL min^{-1}. Sulfuric acid treatment for liquid samples was performed to calculate the olefin yield and selectivity. Eventually, calculations of the catalyst performance were carried out using equations reported in our previous work.[14]

3. RESULTS AND DISCUSSION

3.1. Catalyst Characterization. *3.1.1. Investigation of Thermal Properties Using TGA.* TGA profiles of the as-prepared and pyrolyzed Fe-MIL-88B catalysts were produced under air, as shown in Figure 2. In the TGA curves for

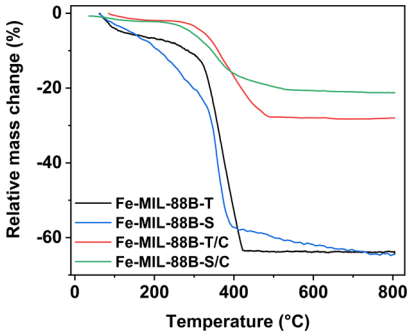

Figure 2. TGA curves for the synthesized MOFs before and after pyrolysis.

precursor MOFs, the first weight loss before 300 °C may be attributed to the evaporation of both solvents, water and DMF. This weight loss is much lower for Fe-MIL-88B-T, indicating better MOF drying activation than that for Fe-MIL-88B-S. A significant weight loss occurred at around 360 °C for Fe-MIL-88B catalysts, caused by the destruction of MOF structures. Hence, to ensure that catalysts were completely pyrolyzed, a temperature of 500 °C was chosen for pyrolysis. TGA curves before and after pyrolysis for both catalysts show relatively similar weight losses, indicating equal Fe concentrations. In addition, as shown in Figure 2, the TGA curves for Fe-MIL-88B-T and Fe-MIL-88B-T/C reached a steady state at lower temperatures than that for Fe-MIL-88B-S and Fe-MIL-88B-S/C. This may be attributed to the fact that Fe-MIL-88B-T could be pyrolyzed at relatively lower temperatures than Fe-MIL-88B-S.

TGA was also used to calculate Fe loading before (in the MOF structure) and after pyrolysis (on the carbon matrix). The residual mass was assumed to be corresponding to Fe_2O_3 only. Fe loadings calculated from TGA were equivalent percentages (about 50 wt %) for both catalysts, as shown in Table 1.

3.1.2. Investigation of Chemical Properties Using FTIR. The IR spectrum of Fe-MIL-88B-S Figure 3a indicates partial coordination of iron ions to the BDC linker. This was confirmed by the strong H_2BDC vibration bands (1687, 1510, 1425, 1292, and 524 cm^{-1}).[67] On the other hand, the IR curve of Fe-MIL-88B-T Figure 3b shows the absence of typical H_2BDC bands (1687 and 524 cm^{-1}), confirming the iron ions' full coordination to the whole BDC linker.[67,68] This explains the lower yield of Fe-MIL-88B-S than that of Fe-MIL-88B-T

https://doi.org/10.1021/acsomega.1c05927
ACS Omega 2022, 7, 8403−8419

Table 1. Fe Loading, Average Particle Size, Textural Properties, and Hydrogen Uptake of Catalysts and Their MOF Precursors

sample	Fe loading[a] (wt %)	average particle size[b] (nm)	S_{BET}[c] ($m^2\ g^{-1}$)	S_{meso}[d] ($m^2\ g^{-1}$)	V_{total}[e] ($cm^3\ g^{-1}$)	V_{meso}[d] ($cm^3\ g^{-1}$)	D_{mean}[f] (nm)	total H_2 consumption[g] (mmol g^{-1})
Fe-MIL-88B-T	24.5	403	457	63	0.23	0.07	2	
Fe-MIL-88B-S	23.7	532	51	51	0.30	0.30	24	
Fe-MIL-88B-T/C	48.9	5.8	108	76	0.45	0.44	18	10
Fe-MIL-88B-S/C	54.5	35.0	105	85	0.38	0.37	15	6

[a]Fe loading as determined by TGA under air. [b]Average particle size calculated by TEM. [c]Total surface area from BET analysis. [d]Mesoporous surface area and volume of mesopores by BJH analysis. [e]Total pore volume at (p/p_0 = 0.990). [f]Mean pore diameter. [g]Total H_2 consumption from TPR analysis.

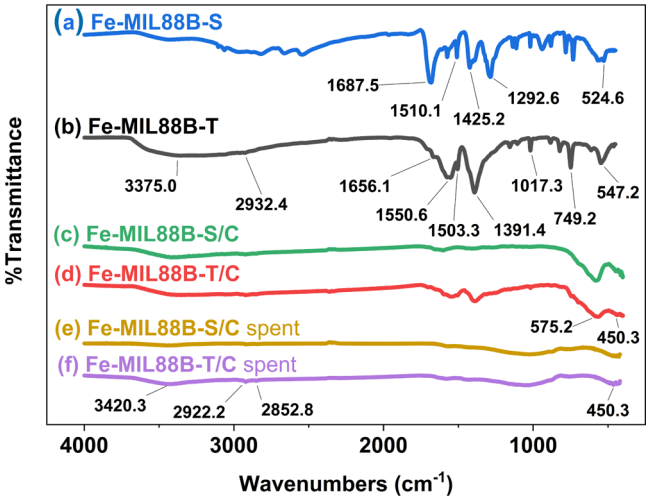

Figure 3. FTIR spectra of samples (a,b) before pyrolysis, (c,d) after pyrolysis, and (e,f) after the reaction.

after synthesis, even using the same molar ratio of precursors. Moreover, H_2BDC remains in the Fe-MIL-88B-S catalyst despite applying the same washing steps for both catalysts, as mentioned in the Experimental Section. The presence of H_2BDC is expected to reduce the surface area of Fe-MIL-88B-S as compared to that of Fe-MIL-88B-T, as discussed later in Section 3.1.5.

We also noticed other strong bands attributed to vibrations of C═O, −COO, C−O, and C−H (1503−1656, 1391, 1017, and 749 cm^{-1}) for both catalysts.[67,68] These observations reaffirm the successful coordination of Fe^{3+} ions with H_2BDC to form MIL-88B crystals for Fe-MIL-88B-T and the incomplete coordination with residual H_2BDC for Fe-MIL-88B-S. For both MOFs, 547 and 3374 cm^{-1} bands, which are typical of Fe−O and O−H vibrations from the adsorbed water molecules, respectively, are evident in Figure 3a,b.[68]

After the pyrolysis of the prepared Fe-MIL-88B MOFs, Figure 3c,d shows a considerable reduction of coordination peaks, implying effective pyrolysis. The strong band observed at 575 cm^{-1} and the weak one at 450 cm^{-1} are analogous to magnetite, as formerly reported,[67,69] while the weak peak at 2932 cm^{-1} could be designated to symmetric C−H vibrations.[69] FTIR spectra after the reaction, as shown in Figure 3e,f, for both catalysts show characteristic bands of Fe_5C_2 (2922 and 2852 cm^{-1}), assigned as stretching vibrations of −CH.[70] In addition, there is no absorption peak known for magnetite at 574 cm^{-1}. The surface of the iron nanoparticles has been modified by OH groups or water molecules (3420 cm^{-1}) produced from FTS, leading to only 450 cm^{-1} Fe−O vibrations peaks.[71]

3.1.3. Investigation of the Crystalline Structure Using XRD. Figure 4a demonstrates the XRD patterns of the MOF catalysts before pyrolysis. The key diffraction peaks for both MOFs at 2-theta (9.16 and 10.50°) are consistent with reported work on Fe-MIL-88B MOF.[36,63] Furthermore, Pu *et al.* demonstrated that complete crystallization is not easy at low temperature (100 °C),[72] which justifies the weak intensities and noise in the background for both XRD patterns.

After pyrolysis (Figure 4b), Fe-MIL-88B-T/C and Fe-MIL-88B-S/C patterns were free of MOF characteristic diffraction peaks, confirming the collapse of the MOF framework. Both XRD patterns indicate that magnetite (Fe_3O_4) is the main iron phase with a face-centered cubic (fcc) structure (JCPDS file,

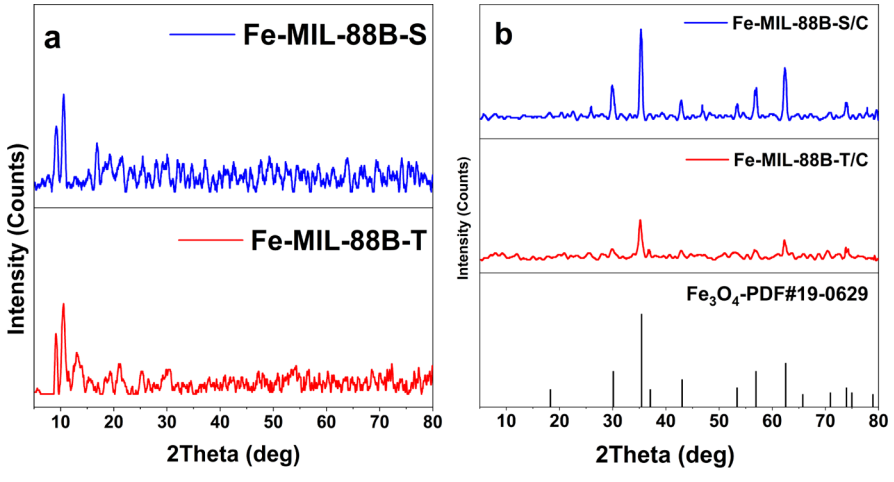

Figure 4. XRD patterns of Fe-MIL-88B-T and Fe-MIL-88B-S before pyrolysis (a) and after pyrolysis (b).

https://doi.org/10.1021/acsomega.1c05927
ACS Omega 2022, 7, 8403−8419

no. 19-0629),[38] which agrees with the FTIR results. However, Fe-MIL-88B-T/C have weaker intensities, which anticipate smaller crystal size.

XRD patterns for the spent Fe-MIL-88B-T/C and Fe-MIL-88B-S/catalysts in Figure 5 show that the main existing phases

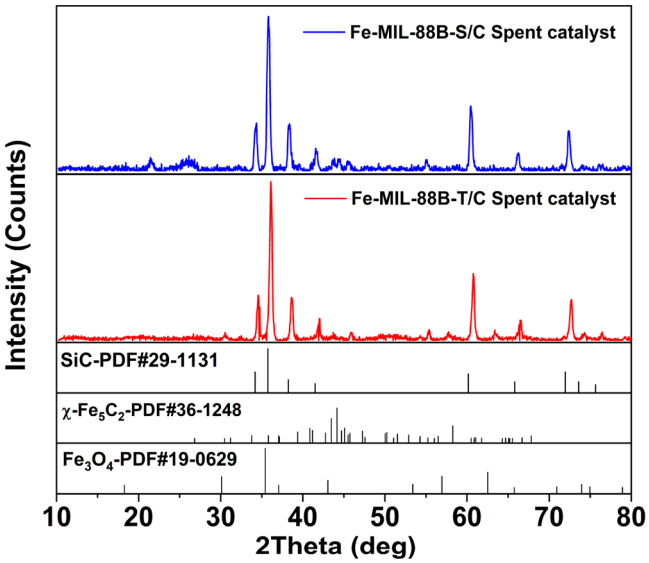

Figure 5. XRD patterns of spent Fe-MIL-88B-T/C and Fe-MIL-88B-S/C catalysts after the FTS reaction.

are Fe_3O_4 and χ-Fe_5C_2 (JCPDS file nos 19-0629 and 36-1248, respectively), which agrees with the FTIR results, in addition to SiC, which was used for the dilution of the catalyst. The absence of the graphite peak for the Fe-MIL-88B-T/C catalyst after 100 h time on stream (TOS) indicates high stability and apparent resistance to carbon deposition. However, a small graphite peak at 25.7° is noticed for the Fe-MIL-88B-S/C catalyst. The graphite peak elucidates carbon deposition, which is one of the deactivation reasons for a long TOS as it masks the active catalytic sites.[73]

3.1.4. Investigation of the Morphological Structure Using SEM and TEM. Figure S1 represents the SEM images of both catalysts before and after pyrolysis. A hexagonal rod morphology is shown in Figure S1b, but it is absent in Figure S1a at equivalent magnification, indicating that Fe-MIL-88B-S crystals have larger sizes than Fe-MIL-88B-T. Furthermore, SEM images of Fe-MIL-88B-T and Fe-MIL-88B-T/C shown in Figure S1a,c at high SEM magnification display an undefined morphology, which confirms smaller particles sizes for Fe-MIL-88B-T/C and agrees with weak magnetite intensities from XRD results.

Figure 6 shows the TEM and high resolution TEM (HRTEM) images of the two Fe-MIL-88B MOFs before and after pyrolysis. Moreover, Figure 7 shows the PSD for both Fe-MIL-88B MOFs before and after pyrolysis. The Fe nanoparticle size range was obtained from TEM based on a sample size of 800−1000 nanoparticles using ImageJ software. Figure 6a shows nonuniform hexagonal rods for Fe-MIL-88B-T of a relatively narrow length distribution (200−600 nm) with the frequent lengths ranging from 200 to 400 nm, as shown in Figure 7a. However, Figure 6b reveals the transformation of the Fe-MIL-88B-T MOF after pyrolysis to small-sized Fe nanoparticles with an average particle size of 5.82 nm with narrow size distribution, as indicated from Figure 7b.

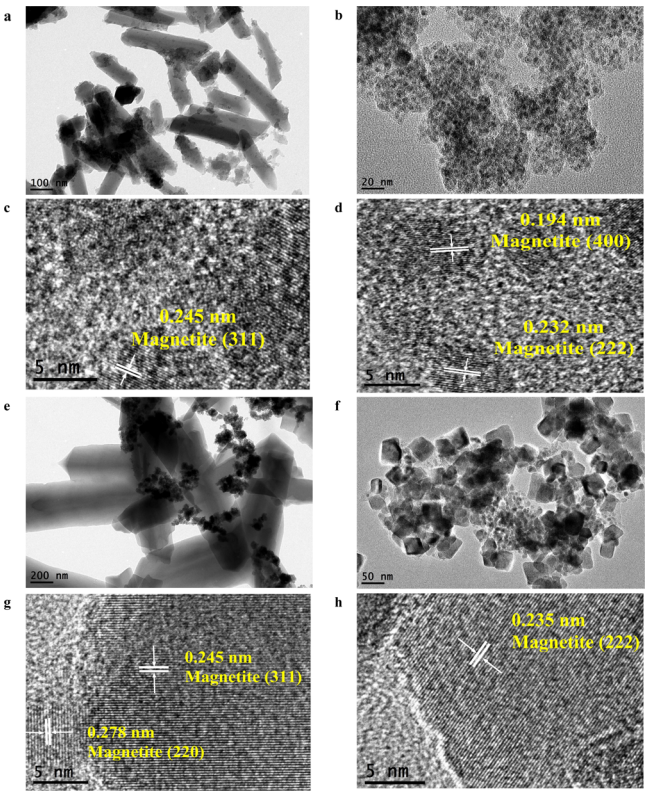

Figure 6. TEM (a,b,e,f) and HRTEM (c,d,g,h) images: (a) Fe-MIL-88B-T, (b−d) Fe-MIL-88B-T/C, (e) Fe-MIL-88B-S, and (g,h) Fe-MIL-88B-S/C.

TEM images of Fe-MIL-88B-S in Figure 6e show a similar hexagonal rod structure but with a wider length distribution (300−1000 nm) with the most frequent range of 400−600 nm, as clarified in Figure 7c. Figure 6f shows that Fe-MIL-88B-S/C has cubic magnetite nanoparticles of wide size distribution with a larger average particle size (35.04 nm) than that of Fe-MIL-88B-T/C, as illustrated in Figure 7d. This indicates that regardless of the use of similar metals and linkers and the same molar ratio, different preparation conditions resulted in MOF crystals with different morphological properties. These properties are somehow inherent in the catalysts stemming from the pyrolysis of fresh MOFs.

The HRTEM images of Fe-MIL-88B-T/C in Figure 6c,d show the interplanar spacings of 0.245, 0.281, 0.232, and 0.194 nm, corresponding to the (311), (220), (222), and (400) lattice planes of the fcc structure of Fe_3O_4, respectively, which supports the XRD results. Likewise, in Figure 6g,h, the HRTEM images of Fe-MIL-88B-S/C show similar interplanar spacings, confirming the XRD results.

High-angle annular dark-field (HAADF)-STEM micrographs and elemental mapping for both catalysts before and after pyrolysis are represented in Figures S2−S5. Elemental mapping of Fe-MIL-88B-T/C, as shown in Figure S4, confirms proper dispersion of iron in the carbon matrix after pyrolysis, which seems to cover more area than that for Fe-MIL-88B-S/C, as shown in Figure S5. Better dispersion exposes more iron to the surface, which is expected to enhance reducibility and activity.

Figures S6 and S8 show the TEM and HRTEM images of both catalysts after the reaction for 100 h TOS, while Figures S7 and S9 show the HAADF-STEM micrographs and

https://doi.org/10.1021/acsomega.1c05927
ACS Omega 2022, 7, 8403−8419

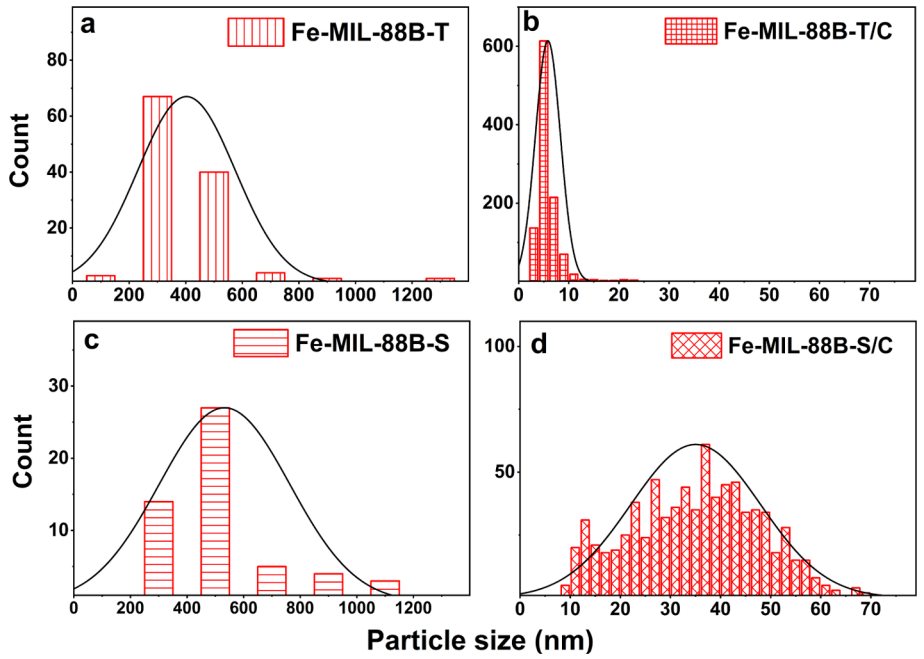

Figure 7. PSD based on TEM images for Fe-MIL-88B-T (a,b) and Fe-MIL-88B-S (c,d) before and after pyrolysis.

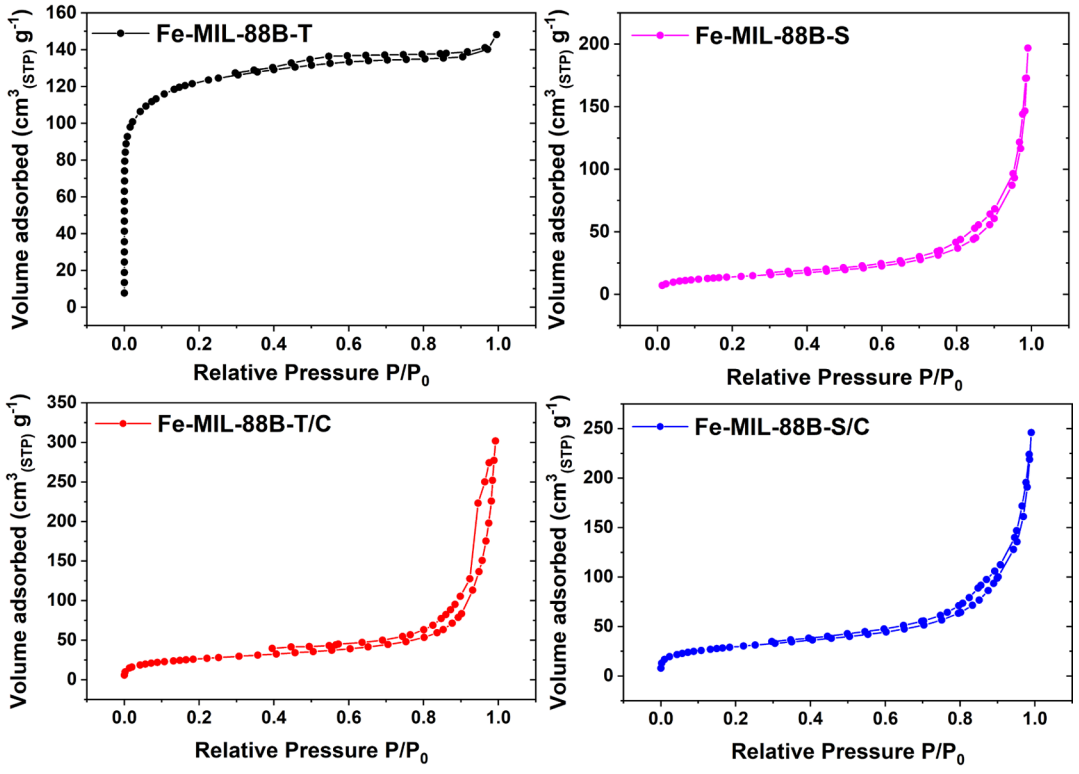

Figure 8. Nitrogen adsorption isotherms of Fe-MIL-88B-T and Fe-MIL-88B-S before and after pyrolysis.

elemental mapping of both spent catalysts. The two catalysts show the unique core/shell structure of Fe_3O_4/χ-Fe_5C_2 reported by An *et al.*, which is advantageous for FTS activity.[36] This is in harmony with HRTEM images containing interplanar spacings corresponding to Fe_3O_4 and χ-Fe_5C_2 (Figures S6 and S8).

Although the XRD data proposes resistance to carbon deposition, amorphous carbon, graphitic carbon, and remarkable carbon nanotubes were noticed in TEM images of spent catalysts in Figures S6 and S8. Amorphous carbon is deposited mainly at LTFT conditions (<280 °C), while graphitic carbon formation is favorable at HTFT conditions (>280 °C), leading to coke deposition.[74] Chen *et al.* studied the effect of graphitic carbon on a cobalt catalyst.[75] The results show a CO conversion decrease due to the suppression of CH_4 formation, an increase in chain-growth probability, and a decrease in olefin hydrogenation.

https://doi.org/10.1021/acsomega.1c05927
ACS Omega 2022, 7, 8403−8419

Alternatively, Ni *et al.* introduced graphitic carbon to an Fe-SiO_2 catalyst where graphite increased the electronic conductivity between Fe and syngas.[76] This resulted in higher CO conversion and light-olefin yield. In addition, it protected the Fe metal from oxidation by eliminating water due to the higher hydrophobic pore surface. However, through the experiments on the iron-based catalyst, Gorimbo *et al.* found that the deposition of graphitic carbon along with the oxidation of the catalyst at long TOS (>1000 h) results in catalyst deactivation.[73]

Amorphous carbon and graphitic carbon were observed in the spent catalyst of Fe-MIL-88B-S/C, whereas carbon nanotubes were observed only in Fe-MIL-88B-T/C besides amorphous carbon and graphitic carbon. Furthermore, the Fe_3O_4/χ-Fe_5C core/shell structure was detected to be confined inside carbon nanotubes, as observed in the TEM images of Figure S6a−d. This exceptional encapsulation enhances the stability of iron carbide nanoparticles by inhibiting sintering.[12]

3.1.5. Investigation of Surface Area and Pore Size Using the BET Method. To elucidate the surface properties of catalysts, BET measurements were performed for the prepared Fe-MIL-88B MOFs before and after pyrolysis. The adsorption−desorption isotherm of Fe-MIL-88B-T in Figure 8 indicates a type-I isotherm, indicative of chemisorption with monolayer adsorption and a microporous structure with a notable sharp increase at very low P/P_0. Conversely, type-IV isotherms are noticeable for the other samples, implying multilayer physisorption and a mesoporous structure.[77] As stated in Table 1, Fe-MIL-88B-T has a larger surface area (457 $m^2\ g^{-1}$) than that of other synthesized products reported in the literature where ferric chloride was used instead of nitrate.[36,63] Unlike the chloride ion that attains an open MIL-88B form, allowing more guest molecules to access pores, the nitrate ion would retain a semi-open form. Guest molecules may cause pore blockage, leading to the loss of porosity and lower surface area.[64,72]

In contrast, with a larger average particle size, as determined from TEM results, Fe-MIL-88B-S possesses a much lower surface area (51 $m^2\ g^{-1}$) even when using a nitrate ion precursor, which is still higher than the values reported in the other work.[63] This could be caused by residual H_2BDC entrapped in its pores or adsorbed on the surface, blocking its porous structure, as confirmed by the FTIR data in Figure 3. The DMF-insoluble Na_2BDC salt, which results from the reaction of H_2BDC with NaOH, could be entrapped in pores or accumulated on the surface of the porous structure of Fe-MIL-88B-S, reducing its surface area and turning its morphology to a mesoporous structure, as shown in Figure 8. Alternatively, TEA produces a DMF-soluble carboxylic form, where MOFs with a highly porous structure are easily obtained.[62] This proves that using TEA as a catalyst for H_2BDC deprotonation positively influences the synthesized MOF's structural properties.

In Table 1, both Fe-MIL-88B-T/C and Fe-MIL-88B-S/C show equivalent surface areas (108 and 105 $m^2\ g^{-1}$, respectively). Fe-MIL-88B-S shows an increase in surface area after pyrolysis, which can be justified by the decomposition of residual H_2BDC entrapped in the porous structure. However, there is a significant loss of Fe-MIL-88B-T surface area after pyrolysis. This can be explained by the collapse of the MOF crystal structure during pyrolysis while being transformed from a microporous structure to a mesoporous structure.[38] Moreover, both catalysts have a modest surface area that is comparable to that of the other published work.[36] The high Fe loading in the catalyst may be the cause leading to a relatively lower surface area.[36,38]

Accordingly, we can say that two opposing forces affect the surface area of the catalyst upon pyrolysis. The decomposition of residual H_2BDC trapped in the pores increases the surface area, while the collapse of the MOF structure decreases the surface area. For Fe-MIL-88B-T/C, the dominant force was the collapse of the MOF structure, which caused an overall decrease in surface area. On the other hand, Fe-MIL-88B-S/C was dominated by the decomposition of the trapped H_2BDC, which caused an increase in the surface area.

Furthermore, as shown in Table 1, the increase in the total pore volume of Fe-MIL-88B-T/C (0.45 $cm^3\ g^{-1}$) and Fe-MIL-88B-S/C (0.38 $cm^3\ g^{-1}$) may be due to the decarboxylation of the BDC linker during the pyrolysis.[78] Both catalysts have a similar mesoporous structure where mesoporous surface area, pore size, and pore volume are equivalent. Additionally, Fe-MIL-88B-T/C shows a hysteresis loop in the adsorption−desorption isotherm in Figure 8. Hysteresis is recognized for well-defined metastable gas adsorption in mesoporous materials at high relative pressures with capillary condensation.[35,38]

3.1.6. Investigation of the Hydrogen Reduction Tendency Using H_2-TPR. Fe-MIL-88B-T/C with enhanced properties such as the high dispersion revealed by elemental mapping and smaller average particle size observed from TEM gives rise to a more accessible metal surface for hydrogen during reduction. This is verified by the TPR results shown in Figure 9. The

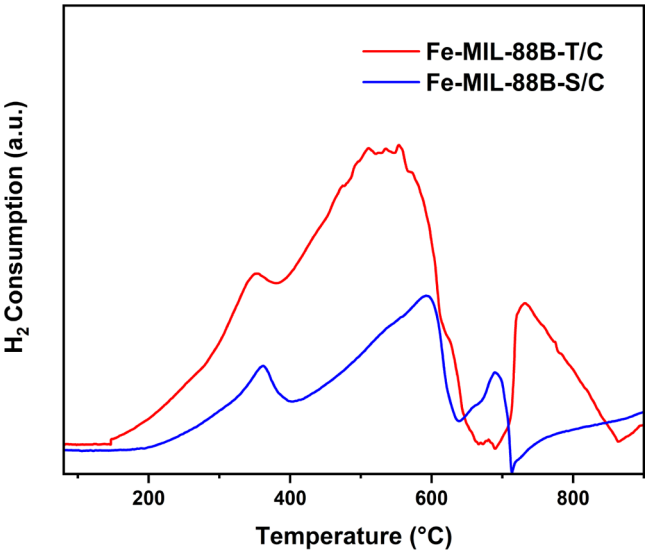

Figure 9. TPR profiles of Fe-MIL-88B-T/C and Fe-MIL-88B-S/C.

more significant hydrogen consumption (10 mmol g^{-1}) than that of Fe-MIL-88B-S/C (6 mmol g^{-1}) indicates higher reducibility. Additionally, the shift of the two prominent reduction peaks of Fe-MIL-88B-S/C to higher temperatures implies the easier reducibility of Fe-MIL-88B-T/C, which starts at relatively lower temperatures. All catalysts undergo two reduction steps where the first two peaks are assigned to the reduction of Fe_3O_4 to FeO and FeO to Fe, respectively. The negative peaks may originate from the breakdown of the residual MOF structure. This is in good agreement with the reduction behavior of iron oxides.[36]

https://doi.org/10.1021/acsomega.1c05927
ACS Omega 2022, 7, 8403−8419

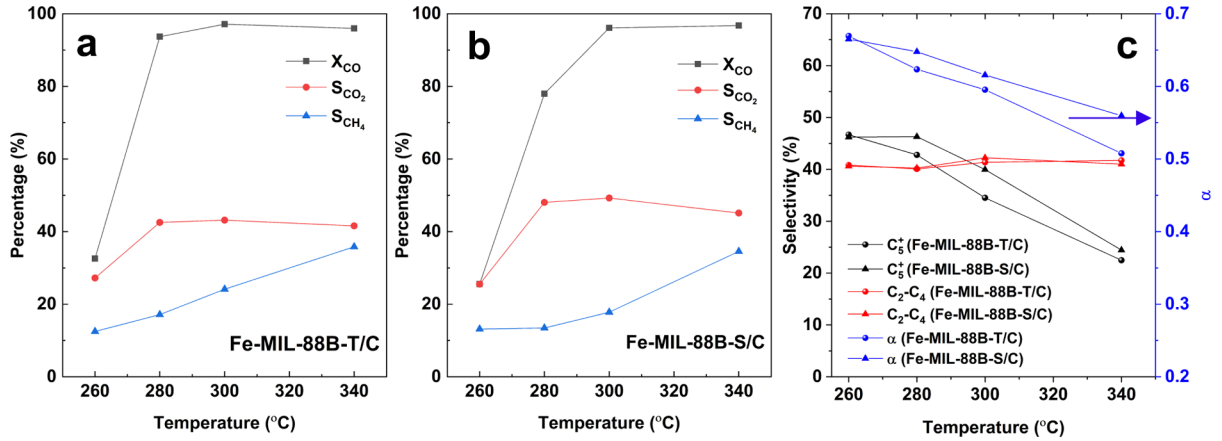

Figure 10. FTS activity as a function of reaction temperature. Carbon monoxide conversion and selectivity of CO_2 and CH_4 for (a) Fe-MIL-88B-T/C and (b) Fe-MIL-88B-S/C. (c) Selectivity of various FTS products and chain growth probability for both catalysts.

Table 2. Comparison of FTS Performance of the Fe-MIL-88B-T/C-Derived Catalyst with That of the Reported Fe-MOF-Derived Catalysts

refs	catalyst (MOF precursor)	P^a (bar)	T^b (°C)	H_2/CO	GHSV (mL g_{cat}^{-1} h^{-1})	X_{CO} (%)	$S_{C_2-C_4^=}$ (%)	$Y_{C_2-C_4^=}$ (%)[g]	Y_{Olefin}[h]
this work	Fe-MIL-88B-T/C	20	280	1	4200	94	22	12	24
33	38-Fe@C (Basolite F300)	20	340	1	60,000	77	14.5[e]	6.0[f]	
36	Fe-MIL-88B/C	20	300	1	36,000	33.8	18.5	4.1	
36	Fe-MIL-88B-NH_2/C	20	300	1	36,000	81.8	21.5	10	
34	Fe@C-500 (Basolite F300)	20	340	1	60,000	76	14[e]	5.5[f]	
35	0.6KFe@C-MIL-68	20	340	1	60,000	41.1			
35	KFe@C-MIL-100	20	340	1	60,000	94.9			
35	Fe@C-MIL-101-NH_2	20	340	1	60,000	65			
35	KFe@C-MIL-88A	20	340	1	60,000	71.3			
35	KFe@C-MIL-127 (MIL-127)	20	340	1	60,000	89.5			
18	Fe/4Na/0.42S-C-Aero (Basolite F300)	10	340	2	48,000	85	52	25.5	
37	Fe@C-500 (Fe-MIL-100)	30	260	2	8000[c]	68	14.5	8.5	
26	Fe@C-600-Reduced (Basolite F300)	20	230	1	55,000	13.9			
38	38Fe@C (Basolite F300)	15	340	1	55[d]	70	13.5	5.5	
40	MIL-101-7 W	20	340	1	13,300[c]	49.86	14.5	5	
40	MIL-101-NH_2-5 W-K	20	340	1	13,300[c]	93.76	24	12	
85	Fe@C-R-1 (Fe-MIL-88B)	20	300	1	36,000	14.05			
39	Fe/CNS(1000) (ZIF-8)	10	340	1	9000	45.9	20.5	6.5	

[a]Syngas pressure. [b]Reactor temperature. [c]Unit: h^{-1}. [d]Unit: $mmol_{CO,\ STP}$ g_{Fe}^{-1} min^{-1}. [e]$S_{C_2-C_5^=}$. [f]$Y_{C_2-C_5^=}$. [g]The olefin yield corrected for CO_2 and unreacted CO. $Y_{C_2-C_4^=}$ (%) $= \frac{S_{C_2-C_4^=} * X_{CO} * (100 - S_{CO_2})}{100 * 100}$. [h]Yield of total olefins.

3.2. FTS Performance Evaluation for Prepared Catalysts. *3.2.1. Effect of Operating Conditions on FTS Performance.* The FTS performance of the two catalysts was studied at various operating conditions of temperature, GHSV, and pressure to obtain the optimum performance in terms of activity and olefin formation. All results are shown in Table S1.

3.2.1.1. Effect of Temperature. Figure 10a,b shows the variation of carbon monoxide conversion (X_{CO}), carbon dioxide selectivity (S_{CO_2}), and S_{CH_4} with temperature for both Fe-MIL-88B-T/C and Fe-MIL-88B-S/C catalysts, respectively. It is clear that X_{CO}, S_{CO_2}, and S_{CH_4} were increased with increasing reaction temperature. At higher temperatures (340 and 300 °C), both catalysts show comparable X_{CO} values. In contrast, at lower temperatures (280 and 260 °C), Fe-MIL-88B-T/C show higher X_{CO} than Fe-MIL-88B-S/C. Furthermore, at all temperature ranges, the Fe-MIL-88B-T/C catalyst produces higher S_{CH_4} and lower S_{CO_2} values. The maximum X_{CO} value for both catalysts at high temperature (97%) is higher than those of most Fe-MOF derived catalysts summarized in Table 2.

Figure 10c demonstrates the disparity of $S_{C_2-C_4}$, C_{5+} selectivity ($S_{C_{5+}}$), and chain growth probability (α) at different reaction temperatures for both catalysts. $S_{C_2-C_4}$ is the same for both catalysts throughout the whole temperature range studied with a minor decrease at lower temperatures for both catalysts. In contrast, $S_{C_{5+}}$ is increasing with decreasing temperature, though it is higher in the case of the Fe-MIL-88B-S/C catalyst except for 260 °C, where both catalysts have the same $S_{C_{5+}}$ selectivity. Likewise, α show the same trend as $S_{C_{5+}}$.

Figure 11 compares the olefin selectivity, O/P ratio, and olefin yield at different reaction temperatures. Both the olefin selectivity and O/P ratio, as illustrated in Figure 11a,b, increase

https://doi.org/10.1021/acsomega.1c05927
ACS Omega 2022, 7, 8403−8419

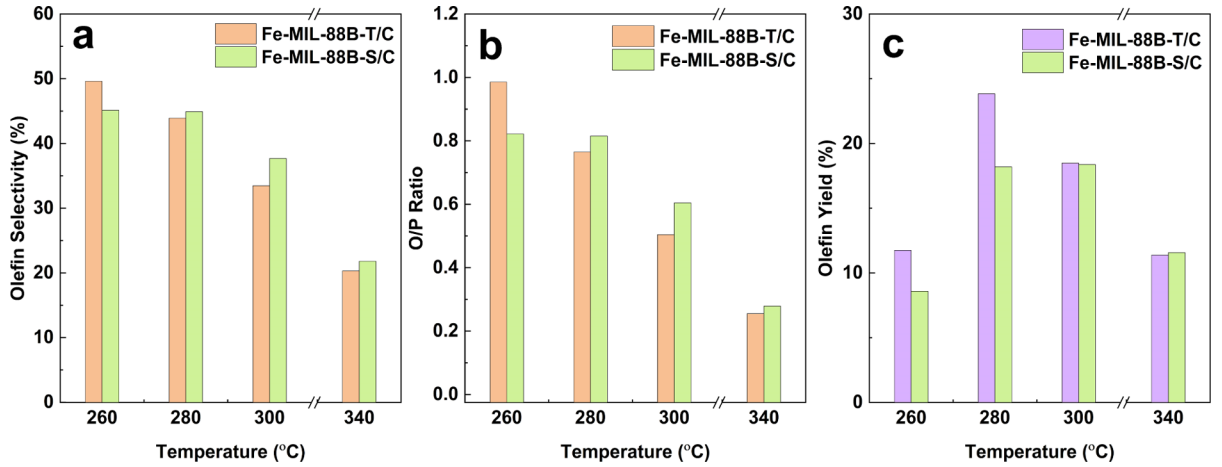

Figure 11. Olefin product comparison over different temperatures for Fe-MIL-88B-T/C and Fe-MIL-88B-S/C. (a) Olefin selectivity. (b) O/P ratio. (c) Olefin yield.

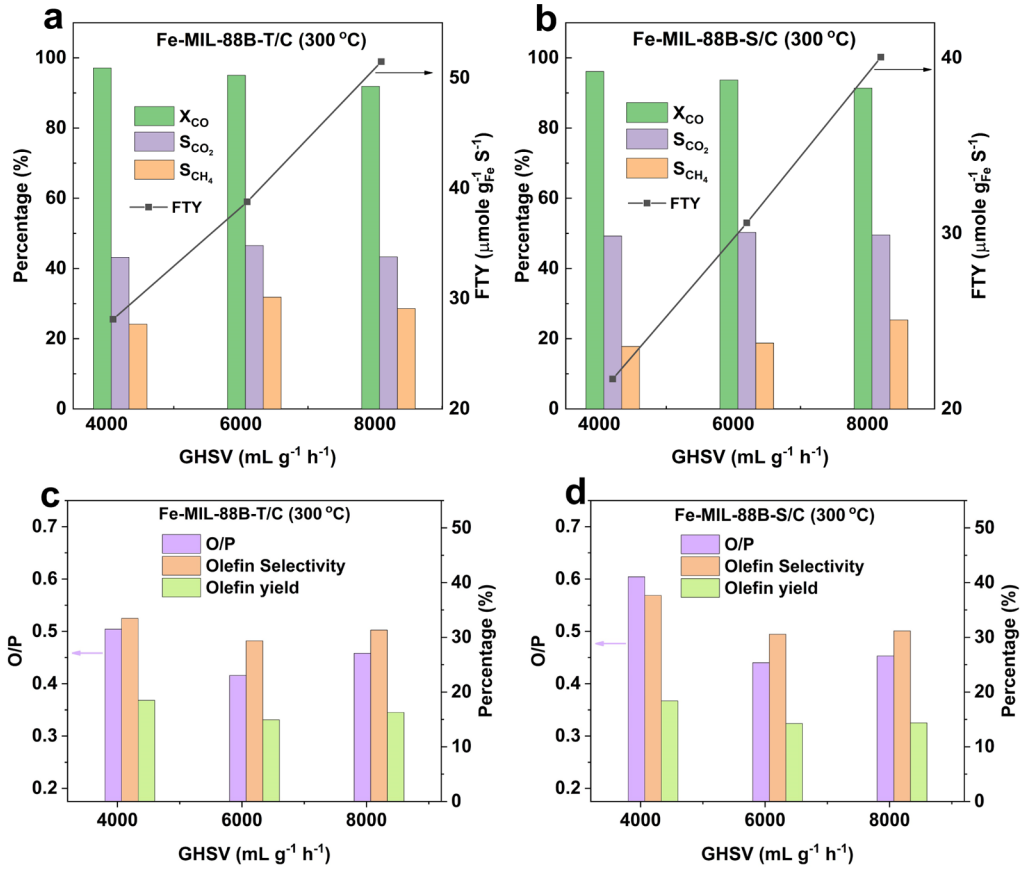

Figure 12. FTS performance as a function of different space velocities. Carbon monoxide conversion and selectivity of CO_2 and CH_4 for (a) Fe-MIL-88B-T/C and (b) Fe-MIL-88B-S/C. Olefin selectivity, O/P ratio, and olefin yield for (c) Fe-MIL-88B-T/C and (d) Fe-MIL-88B-S/C.

with decreasing temperature. It is well-known that the temperature changes the reaction rate constant depending on the activation energy. Therefore, temperature modification could alter the FTS product selectivity by allowing secondary reactions to primary products such as olefin hydrogenation.[79] For example, at high X_{CO}, olefins are exposed to more hydrogen and get hydrogenated, increasing paraffin selectivity.[80] The individual olefin selectivity and O/P values for both catalysts at all temperatures were close enough (about 5% difference) that a distinction between them is not observable. Alternatively, it is clear that olefin yield peaks at medium temperatures (280 and 300 °C), showing a decrease at lower and higher temperatures, as shown in Figure 11c.

Olefin yield is directly proportional to X_{CO} and olefin selectivity but inversely proportional to S_{CO_2}. At lower temperatures (<280 °C), even though the olefin selectivity is at its maximum value, the olefin yield is low. This is due to the drop in X_{CO} at low temperatures due to the reduced catalyst activity. Moreover, S_{CO_2} decreased at low temperatures, and it

https://doi.org/10.1021/acsomega.1c05927
ACS Omega 2022, 7, 8403−8419

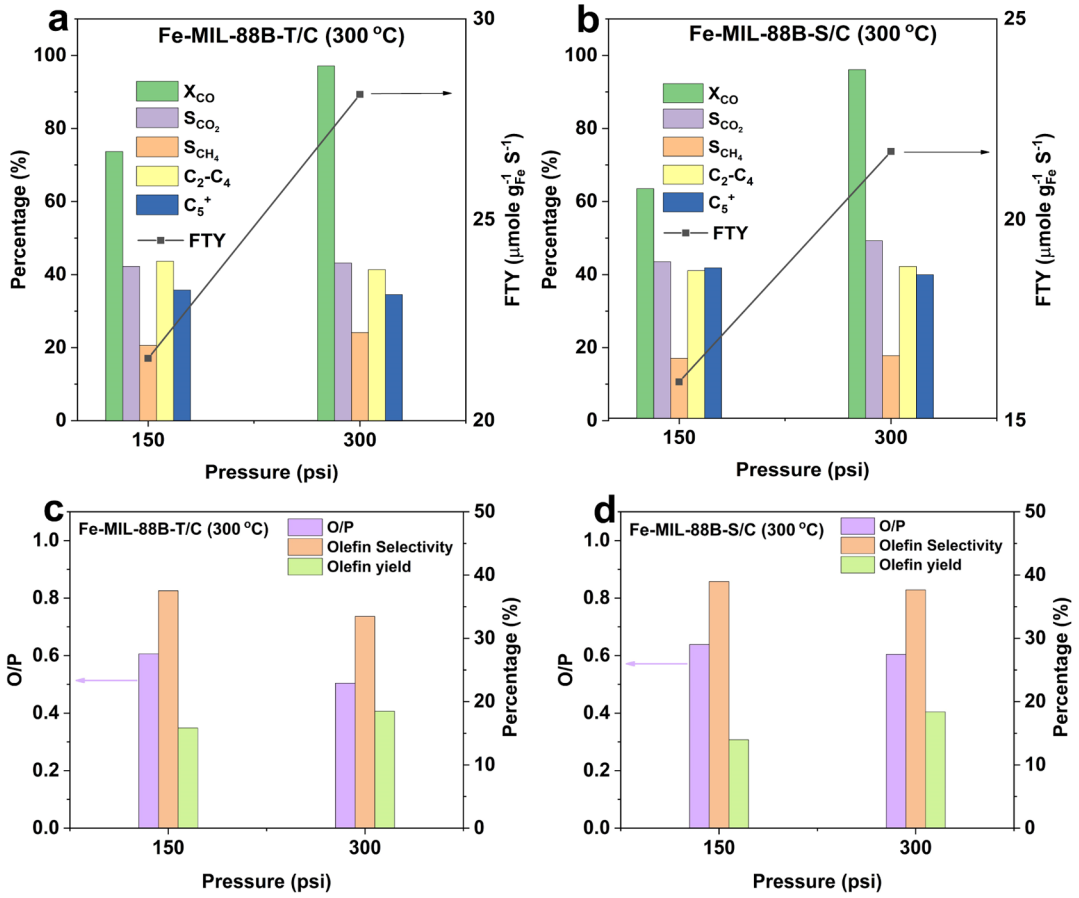

Figure 13. FTS performance as a function of pressure. Carbon monoxide conversion, product selectivity, and FTY for (a) Fe-MIL-88B-T/C and (b) Fe-MIL-88B-S/C. Olefin selectivity, O/P ratio, and olefin yield for (c) Fe-MIL-88B-T/C and (d) Fe-MIL-88B-S/C.

was expected to cause an increase in olefin yield; however, its effect was weaker than the effect of the drop in X_{CO}.

At 280 °C, the olefin yield reaches its maximum value (19% for Fe-MIL-88B-S/C and 24% for Fe-MIL-88B-T/C). This is caused by the sharp increase in $X_{CO,}$ which jumped from 26% at 260 °C to 78% at 280 °C for Fe-MIL-88B-S/C and from 33% at 260 °C to 94% at 280 °C for Fe-MIL-88B-T/C. This sharp increase overcame the decrease in olefin selectivity and theincrease in S_{CO_2} that happened between 260 and 280 °C. At higher temperatures (>280 °C), olefin yield decreased again, reaching 12% at 340 °C for both catalysts. This is mainly due to the olefin selectivity decline since X_{CO} and S_{CO_2} values are stable above 280 °C. Thus, it can be observed that the optimum condition for the maximum olefin productivity with our catalysts is in the vicinity of 280 °C.

3.2.1.2. Effect of GHSV. Figure 12 illustrates the effect of GHSV on FTS performance for both catalysts. Figure 12a,b indicates a slight decrease in X_{CO}, accompanied by an increase in S_{CH_4} and FTY with increasing GHSV. Additionally, there was a decrease in $S_{C_{5+}}$, as listed in Table S1 and indicated by the values of α. The FTY value for Fe-MIL-88B-T/C is constant at 340−280 °C (28 μmol_{CO} g_{Fe}^{-1} s^{-1}) after 16−18 h TOS with a GHSV of 4200 mL g_{cat}^{-1} h^{-1} and a pressure of 20 bar. The FTY value can be increased to 51 μmol_{CO} g_{Fe}^{-1} s^{-1} after increasing the GHSV to 8200 mL g_{cat}^{-1} h^{-1} and expected to be boosted even more at higher GHSV values, comparable to those in the reported literature.[26,33−36,38]

Figure 12c,d illustrates the effect of increasing the GHSV on the olefin productivity of the catalyst as expressed by the olefin selectivity, O/P ratio, and olefin yield. It was expected that increasing the GHSV would slightly negatively affect olefin productivity, which is evident from Figure 12c,d. This is because increasing GHSV will increase the supply of feed gas to the catalyst surface, increasing the surface concentration of the surface hydrogen. A high hydrogen concentration would shift the product spectrum toward paraffin and away from olefins, which agrees with our previous findings.[14]

3.2.1.3. Effect of Pressure. Figure 13 demonstrates the effect of pressure on catalytic performance for both catalysts. Decreasing the pressure triggers a decrease in X_{CO}, FTY, and olefin yield while increasing the olefin selectivity and O/P ratio. The increase in olefin selectivity with decreasing pressure is because olefin hydrogenation is favored at higher pressures.[16] Furthermore, Fe-MIL-88B-T/C has higher X_{CO}, olefin yield, and FTY than Fe-MIL-88B-S/C while having a lower $S_{C_{5+}}$ and comparable olefin selectivity and O/P ratio values.

3.2.2. Selectivity of Olefin Fraction Production from FTS. Figure 14a−d describes the change in the olefin selectivity and O/P ratio with temperature for both catalysts. It can be observed in Figure 14a,c that, in general, the overall olefin selectivity decreases with temperature, as mentioned before, and the same applies for the C_2−C_4 and C_5−C_{13} fractions. It can also be noticed that at all temperatures and for both catalysts, $S_{C_2-C_4^=}$ is always higher than $S_{C_5-C_{13}^=}$. When looking at

https://doi.org/10.1021/acsomega.1c05927
ACS Omega 2022, 7, 8403−8419

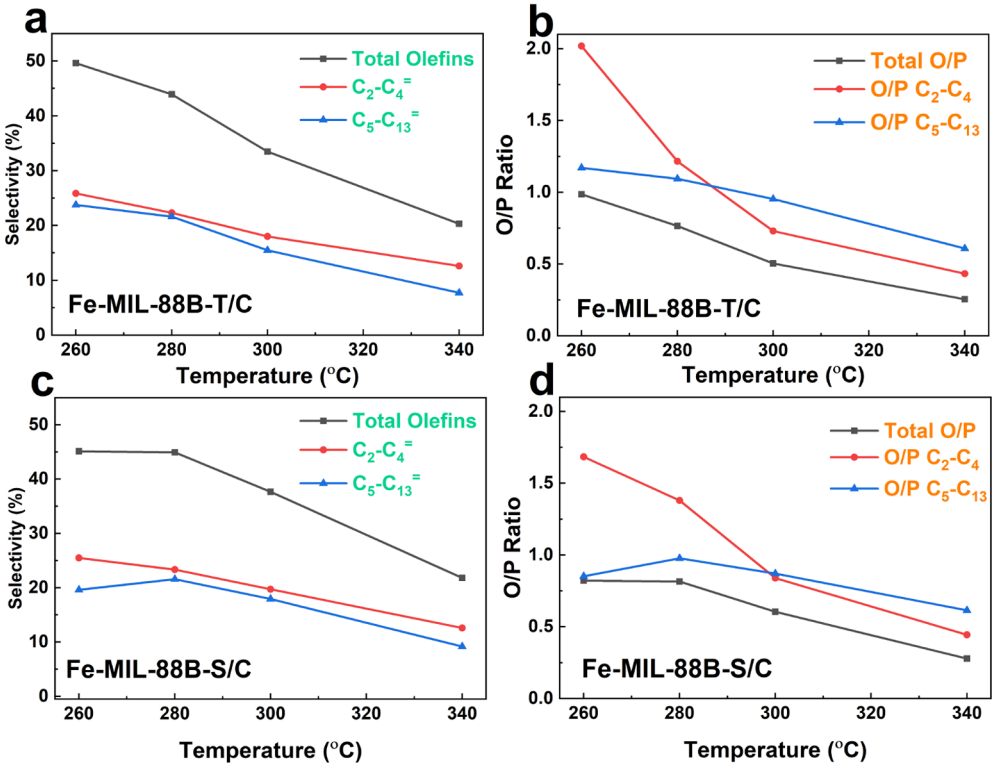

Figure 14. Olefin product distribution as a function of reaction temperature. Olefin selectivity and O/P ratio of (a,b) Fe-MIL-88B-T/C and (c,d) Fe-MIL-88B-S/C.

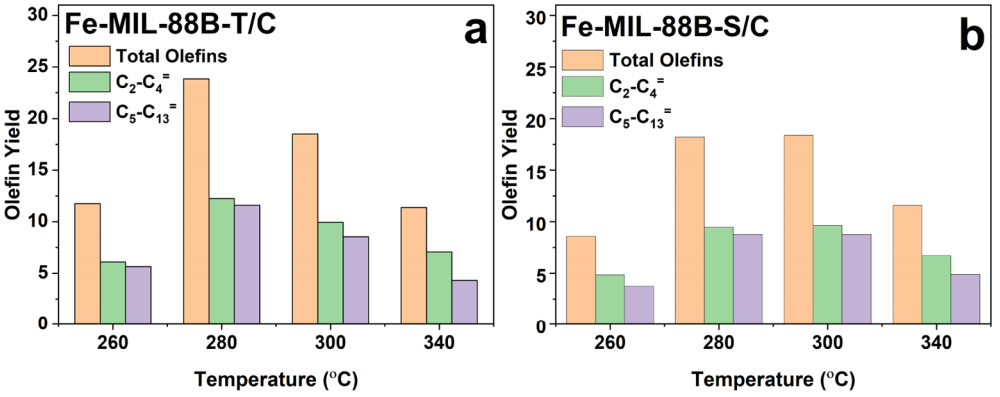

Figure 15. Olefin yield product distribution as a function of reaction temperature for (a) Fe-MIL-88B-T/C and (b) Fe-MIL-88B-S/C.

the O/P ratio curves in Figure 14b,d, it is clear that the curves for the overall O/P ratio and the C_5-C_{13} O/P ratio show a steady decline with the increase in temperature for both catalysts. However, an interesting feature is noticed when looking at the O/P ratio curves for the C_2-C_4 fraction. The O/P ratio for this fraction decreases sharply beyond 280 °C for both catalysts. This means that below 280 °C, the C_2-C_4 fraction is rich in olefins with an O/P ratio ranging from 1.7 for Fe-MIL-88B-S/C to 2 (67%) for Fe-MIL-88B-T/C at 260 °C. Also, when comparing Figures 14b,d and 10a,b, a link can be constructed between the sudden drop in the X_{CO} and the sudden increase in the O/P ratio for the C_2-C_4 fraction below 280 °C. It is as if the O/P ratio for the C_2-C_4 fraction mimics the behavior of the X_{CO}.

It can be stated that lower temperatures favor olefin production over paraffin due to the decrease in catalyst activity and surface concentration of hydrogen formed by the dissociative adsorption of H_2. This decrease in hydrogen concentration lowers the surface H/C ratio, favoring olefin formation with a lower H/C ratio.[80] Thus, it was expected that the O/P ratio would increase as temperature decreases. Furthermore, the temperature drop is known to cause an increase in the average molecular weight of the product, favoring the formation of heavier hydrocarbons and increasing the C_{5+} fraction, as indicated by the change in alpha with temperature shown in Figure 10c. It is also worth noting that the number of possible isoparaffins decreases as the hydrocarbon chain length decreases. In addition, the natural ability of the C_5-C_{13} fraction to form isoparaffins is fundamentally higher than that of the C_2-C_4 fraction, which has a limited number of possible isoparaffins.

When these three factors are combined, it can be understood why there is a sudden increase in the O/P ratio for the C_2-C_4 fraction below 280 °C. The low temperature increased the

https://doi.org/10.1021/acsomega.1c05927
ACS Omega 2022, 7, 8403−8419

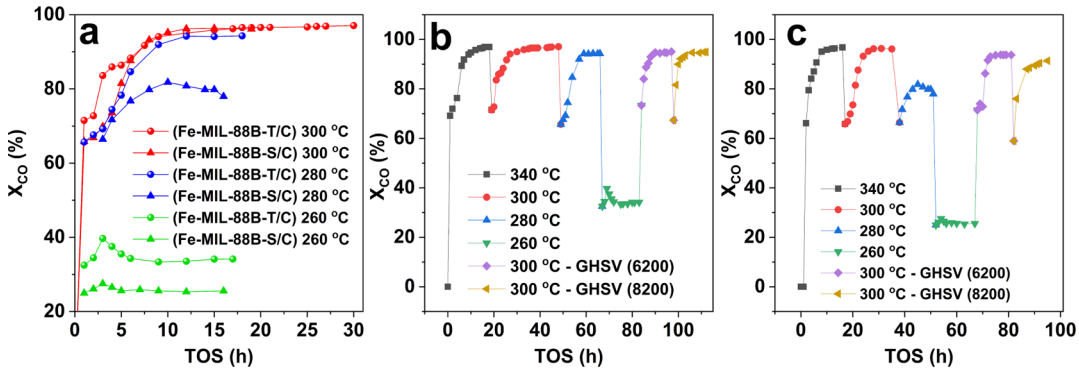

Figure 16. Catalytic performance stability. (a) Carbon monoxide conversion for a reaction time of 16−30 h over different temperatures. Carbon monoxide conversion as a function of various operating conditions for a reaction time of 100 h or more for (b) Fe-MIL-88B-T/C and (c) Fe-MIL-88B-S/C.

olefin selectivity and the heavier hydrocarbon selectivities simultaneously, which means that at low-temperature, productivity is oriented toward olefins and heavy hydrocarbons. Also, since the C_2−C_4 fraction is a light fraction (unfavored at low temperature) with a low number of possible isoparaffins, the paraffin productivity is expected to fall sharply at low temperature while enhancing the olefin productivity. This all causes the O/P ratio for the C_2−C_4 to increase dramatically at temperatures below 280 °C.

Following the trend of olefin selectivity, the olefin yield of C_2−C_4 is higher than that of C_5−C_{13} in the entire temperature range, as presented in Figure 15. More importantly, the difference gap between the olefin yields of C_2−C_4 and C_5−C_{13} increase with increasing temperature. Thus, when targeting light olefins, increasing the temperature is helpful for an orientation toward higher light olefin formation. The olefin yield of C_2−C_4 reaches its maximum (12%) at 280 °C for Fe-MIL-88B-T/C and at 280−300 °C (9%) for Fe-MIL-88B-S/C. This value for Fe-MIL-88B-T/C is more significant than that of most Fe-MOF derived catalysts used in FTS (Table 2) and comparable to that in the other work, especially for promoted catalysts.

3.2.3. Evaluation of the FTS Catalytic Stability of the Prepared Fe-MIL-88B-Based Catalysts. Figure 16a compares the X_{CO} of both catalysts versus the TOS. At higher temperatures (340 and 300 °C), both catalysts retain X_{CO} for TOS values of up to 30 h. Alternatively, at lower temperatures, Fe-MIL-88B-T/C shows relatively higher X_{CO} retention with better stability than Fe-MIL-88B-S/C. This verified by the small graphitic peak observed for the spent Fe-MIL-88B-S/C catalyst, as shown in Figure 5, and is in line with the deactivation mechanism by graphitic carbon discussed by Gorimbo *et al.* and Chen *et al.*[73,75]

To confirm the stability of both catalysts, a series of continuous catalytic tests were performed with varying temperatures and GHSVs for more than 100 h. Figure 16b,c shows satisfactory stability of both catalysts at various operating conditions for TOS values of up to 100 h or more. This is confirmed by XRD results where there are no obvious peaks for carbon deposition in the spent MIL-88B-T/C catalyst. Despite the graphitic deposition noticed in the MIL-88B-S/C catalyst, it shows good stability except for lower temperatures.

3.2.4. Comparison of the FTS Performance of the Prepared Fe-MIL-88B-Based Catalysts. Figure 17 illustrates the differences between the two catalysts in X_{CO}, hydrocarbon

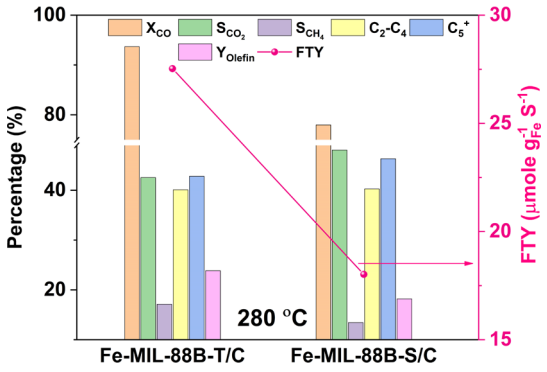

Figure 17. Catalytic performance comparison between Fe-MIL-88B-T/C and Fe-MIL-88B-S/C at 280 °C, 20 bar, and a GHSV of 4200 mL g_{cat}^{-1} h^{-1}.

selectivity, olefin yield, and FTY at 280 °C. The optimum performance of Fe-MIL-88B-T/C was attained at 280 °C, where it maintained a high X_{CO} (94%) compared to the X_{CO} (78%) of Fe-MIL-88B-S/C while reaching comparable olefin selectivity. In addition, Fe-MIL-88B-T/C has a 1.5-fold higher FTY and a 1.26-fold higher olefin yield than Fe-MIL-88B-S/C at this temperature.

Although there are similarities between the two prepared Fe-MIL-88B MOFs, they have several different properties. Some of these were inherited after pyrolysis of MOFs and were observed by characterizations, including the weight yield of the synthesized MOF, particle size, and hydrogen uptake. This is manifested by the different FTS performances of the two catalysts, as shown in the previous sections. According to the literature, iron particle size is one of the parameters that has a profound effect in nanocatalysis, especially on FTS performance, including X_{CO}, S_{CO_2}, S_{CH_4}, hydrocarbon selectivity, and FTY.[42,44] As noticed from the TEM data of this work, the average iron particle size of Fe-MIL-88B-T/C (5.8 nm) is far smaller than that of Fe-MIL-88B-S/C (35.0 nm). In general, Fe-MIL-88B-T/C shows higher X_{CO} percentages than Fe-MIL-88B-S/C. In addition, this agrees with the TPR results, where the H_2 uptake of the Fe-MIL-88B-T/C catalyst is 2-fold higher than that of the Fe-MIL-88B-S/C catalyst, as presented in Table 1. This is also in harmony with the effect of smaller particle size found in the literature.[12,34,81,82]

Smaller iron particles have a higher active phase surface area.[58] Subsequently, the adsorption of syngas feed on the catalyst increases and so does the catalyst reduction and FTS

https://doi.org/10.1021/acsomega.1c05927
ACS Omega 2022, 7, 8403−8419

activity. Furthermore, smaller iron particles accelerate the active iron carbide formation.[47] In their study on promoted and unpromoted Fe catalysts for HTFT synthesis, Gu *et al.*[12] reported that X_{CO} of the unpromoted catalyst reaches its maximum at a threshold particle size of 6 nm and it remains constant above this threshold. This is different from promoted catalysts whose X_{CO} values decrease with particle sizes above 6 nm. This agrees with our results at higher temperatures with similar X_{CO} values for both Fe-MIL-88B-T/C (5.8 nm) and Fe-MIL-88B-S/C (35.0 nm) catalysts.

On the other hand, Park *et al.*[51] studied iron catalysts with different particle sizes at low temperatures and showed the same X_{CO} trend as that suggested by Gu *et al.*[12] for particle sizes below 6 nm. However, Park *et al.*[51] proved that X_{CO} decreases for larger particles above 6 nm due to the reduced active surface area of the iron metal. Our results demonstrate this at lower temperatures where X_{CO} values with the larger particle Fe-MIL-88B-S/C catalyst are lower than that for Fe-MIL-88B-T/C. The increase in Fe-MIL-88B-T/C catalytic activity is also supported by findings from elemental mapping and TPR showing higher dispersion and reducibility of iron particles. Other studies were performed at low temperature and are consistent with our results.[51,81,82]

As iron particle size decreases, surface hydrogen adsorption increases, leading to high C1 monomer concentration and more CH_χ coverage, which increases S_{CH_4} and lowers chain growth probability.[52,54] Smaller particle size has a higher affinity to adsorb hydrogen than CO, leading to more hydrogen at the surface, which eventually generates CH_4 or light hydrocarbons, implying lower $S_{C_{5+}}$ values.[51] Furthermore, higher CH_χ coverage indicates increased FTY, as demonstrated by Torres Galvis *et al.*[52] and Tu *et al.*[81] for promoted and unpromoted catalysts with decreasing size at all temperatures. This is evident in our work as Fe-MIL-88B-T/C shows relatively higher S_{CH_4}, lower $S_{C_{5+}}$, and higher FTY values than Fe-MIL-88B-S/C. This is also confirmed by other studies in the literature.[12,50−52] On the other hand, larger particles have lower surface H coverage, producing lower S_{CH_4} and higher $S_{C_{5+}}$, α, and light olefins.[50,81] The increase in $S_{C_{5+}}$ and α is confirmed by other reported studies.[51,81,82]

Torres Galvis *et al.*,[52] Gu *et al.*,[12] and Liu *et al.*[55] showed similar conclusions in their work on the influence of iron particle size on the production of light olefins. For the promoted catalyst, the light olefin selectivity and O/P ratio tend to correlate with increasing particle size above 6 nm. For the unpromoted catalyst, the size of iron nanoparticles does not significantly affect the olefin selectivity and O/P ratio. This is comparable with our results as both catalysts without promoters show insignificant differences in the olefin selectivity and O/P ratio with various particle sizes.

Interestingly, Fe-MIL-88B-T/C shows higher olefin yield values than Fe-MIL-88B-S/C at lower temperatures, especially at 280 °C since Fe-MIL-88B-S/C has a higher S_{CO_2} and lower X_{CO} values. It is necessary to point out here that the reason behind Fe-MIL-88B-T/C reaching a higher olefin yield value at 280 °C can be explained by looking at Figure 10a,b, where Fe-MIL-88B-T/C shows a faster increase in X_{CO} with temperature than Fe-MIL-88B-S/C. This enables the catalyst to carry out the FTS reaction at higher conversions with a low enough temperature to allow for higher olefin selectivity, which is manifested in the higher olefin yield value. This interesting performance can be attributed to using TEA in the preparation method, which endows the catalyst with smaller particle size and higher FT activity, as evident from TEM, PSD, and TPR results. As a future work and based on previous findings,[12,52] it is expected that the promotion of Fe-MIL-88B-T/C and Fe-MIL-88B-S/C will significantly affect the catalytic activity and light olefin selectivity.

The iron particle size also may affect the MSI. The thermal stability of the metal on its support is vital to avoid sintering, and it might depend on its particle size. The thermal stability increases as particle size increases to a limit beyond which metal nanoparticles could be prone to sintering.[83] Campbell *et al.* demonstrated that the surface adsorption energy of a metal atom increases as the particle size decreases below 6 nm. When particle size exceeds 6 nm, catalyst sintering is more likely to occur as the surface energy decreases.[84] In addition, larger Fe particles are more vulnerable to phase change and carbon deposition, leading to less stability.[33] Furthermore, a narrow range distribution of particle sizes can obstruct sintering through the Ostwald ripening, which involves the migration of different particle sizes (broad distribution) to form a larger particle.[83] Unlike the Fe-MIL-88B-S/C catalyst, Fe-MIL-88B-T/C shows a narrow distribution with small average particle size, as shown in Figure 7. However, both catalysts show reasonable stability with a TOS of up to 100 h or more, see Figure 16b,c.

3.2.5. Comparison with Previous Studies. Because the used catalysts in this work are derived from the Fe-MIL-88B MOF and are tested to optimize olefin yield, it is interesting to compare them with various Fe-MOF-derived catalysts reported in the literature (Table 2). As observed from Table 2, the X_{CO} values for both catalysts at high temperatures (97%) are higher than that of most reported unpromoted Fe-MOF-derived catalysts. Likewise, the X_{CO} value (94%) at 280 °C is higher than those listed in studies at higher temperatures. This may be because the majority of literature studies apply much higher GHSV values than the values used in this work. One of the most remarkable outcomes is that the light olefin yield and selectivity of Fe-MIL-88B-T/C (12 and 22%, respectively) are higher than those in some studies while being comparable to those in other studies on promoted catalysts.

The use of different catalysts and different operating conditions, such as GHSV and pressure, makes the comparison more difficult. For instance, Oschatz *et al.*[18] studied an Fe-BTC-derived catalyst with a large pore volume (1.18 $cm^3\ g^{-1}$) and a Na promoter. This catalyst was tested under operating conditions of a lower pressure (10 bar) and a higher GHSV (48,000 mL $g_{cat}^{-1}\ h^{-1}$). All these parameters together, which were not used in our study, favored the production of light olefins, reaching values larger than our results by 2-fold, with values of 52 and 25.5% olefin selectivity and yield, respectively. Alternatively, our results are relatively higher than those of An *et al.*[36] and Nisa *et al.*,[85] where the catalyst and operating conditions similar to those in our work were applied, except for the GHSV (36,000 mL $g_{cat}^{-1}\ h^{-1}$). It was noted that the total olefin yield was not stated in all previous studies listed in Table 2, while in this work, it was as high as 24% for Fe-MIL-88B-T/C at 280 °C for a total olefin selectivity of 44%. More importantly, all the obtained promising results in this work are on unpromoted catalysts. It is well-known that promoters enhance the catalytic activity and olefin production.

https://doi.org/10.1021/acsomega.1c05927
ACS Omega 2022, 7, 8403−8419

4. CONCLUSIONS

Preparation of an Fe-MIL-88B-derived catalyst was found to be influenced by the modification in the synthesis method used. Using TEA instead of NaOH as a deprotonation catalyst increased MOF synthesis yield and favored smaller crystal formation. After the MOF was pyrolyzed, smaller iron particles with a size of 6 nm were obtained using TEA despite the high Fe loading (50%). Thus, the two MOFs were obtained with similar structures but with different particle sizes. Smaller iron particle size enhances dispersion and reducibility, which affects catalytic activity and product distribution.

Consequently, smaller particle size boosted carbon monoxide conversion up to 94% at 280 °C (*vs* X_{CO} = 78% for larger particle size) with a maximum olefin yield value of 24% and good stability for more than 100 h. Furthermore, higher H-radical coverage for a catalyst with smaller particles resulted in higher CH_4 selectivity and FTY and lowered chain growth probability. The reflected performance, without the help of any promoters, fosters the potential for future study employing a promoted catalyst with expected higher catalytic activity and olefin yield. Among the contradicting literature studies, this study, where other overlapping variables were kept constant, provides new evidence of the iron particle size effect on FTS performance and insights into maximizing the economically valuable olefinic products.

■ ASSOCIATED CONTENT

Supporting Information

The Supporting Information is available free of charge at https://pubs.acs.org/doi/10.1021/acsomega.1c05927.

SEM images of catalysts before and after pyrolysis, TEM and HRTEM images of spent catalysts, EDX elemental mapping of all materials, and catalysts' FTS performance under various operating conditions (PDF)

■ AUTHOR INFORMATION

Corresponding Authors

Ahmed E. Rashed − *Basic and Applied Science Institute, Egypt-Japan University of Science and Technology, New Borg El-Arab 21934, Egypt; Environmental Sciences Department, Faculty of Science, Alexandria University, Alexandria 21511, Egypt;* orcid.org/0000-0002-6465-1406; Email: ahmed.abdeldayem@ejust.edu.eg

Ahmed Abd El-Moneim − *Basic and Applied Science Institute, Egypt-Japan University of Science and Technology, New Borg El-Arab 21934, Egypt*; Email: ahmed.abdelmoneim@ejust.edu.eg

Authors

Alhassan Nasser − *Chemical Engineering Department, Faculty of Engineering, Alexandria University, Alexandria 11432, Egypt*

Marwa F. Elkady − *Chemical and Petroleum Engineering Department, Egypt-Japan University of Science and Technology, New Borg El-Arab 21934, Egypt; Fabrication Technology Department, Advanced Technology and New Materials Research Institute (ATNMRI), City of Scientific Research and Technological Applications, Alexandria 21934, Egypt*

Yoshihisa Matsushita − *Egypt-Japan University of Science and Technology, New Borg El-Arab 21934, Egypt*

Complete contact information is available at: https://pubs.acs.org/10.1021/acsomega.1c05927

Notes

The authors declare no competing financial interest.

■ ACKNOWLEDGMENTS

The authors thank the Mission Sector-MOHE for funding the PhD degree for the first author, the Japan International Cooperation Agency (JICA) and Basic and Applied Sciences Institute at EJUST for providing laboratories, analysis, and materials needed for this work. This work was done as a part of the research project titled "Green Integrated Solar Fuel Production System: Two steps and Direct FT Synthesis Routes", (ID: 7825), supported by the Academy of Scientific Research and Technology (ASRT) in Egypt.

■ REFERENCES

(1) Zhang, Q.; Hu, S.; Chen, D. A Comparison between Coal-to-Olefins and Oil-Based Ethylene in China: An Economic and Environmental Prospective. *J. Clean. Prod.* **2017**, *165*, 1351−1360.

(2) Boulamanti, A.; Moya, J. A. Production Costs of the Chemical Industry in the EU and Other Countries: Ammonia, Methanol and Light Olefins. *Renew. Sustain. Energy Rev.* **2017**, *68*, 1205−1212.

(3) Sanhoob, M. A.; Khalil, U.; Shafei, E. N.; Choi, K.-H.; Yokoi, T.; Muraza, O. Steam Cracking of Green Diesel (C12) to BTX and Olefins over Silane-Treated Hierarchical BEA. *Fuel* **2020**, *263*, 116624.

(4) Lima, D. S.; Perez-Lopez, O. W. Oxidative Coupling of Methane to Light Olefins Using Waste Eggshell as Catalyst. *Inorg. Chem. Commun.* **2020**, *116*, 107928.

(5) Dimian, A. C.; Bildea, C. S. Energy Efficient Methanol-to-Olefins Process. *Chem. Eng. Res. Des.* **2018**, *131*, 41−54.

(6) Torres Galvis, H. M.; Koeken, A. C. J.; Bitter, J. H.; Davidian, T.; Ruitenbeek, M.; Dugulan, A. I.; de Jong, K. P. Effect of Precursor on the Catalytic Performance of Supported Iron Catalysts for the Fischer-Tropsch Synthesis of Lower Olefins. *Catal. Today* **2013**, *215*, 95−102.

(7) Sun, J.; Yang, G.; Peng, X.; Kang, J.; Wu, J.; Liu, G.; Tsubaki, N. Beyond Cars: Fischer-Tropsch Synthesis for Non-Automotive Applications. *ChemCatChem* **2019**, *11*, 1412−1424.

(8) Shafer, W.; Gnanamani, M.; Graham, U.; Yang, J.; Masuku, C. M.; Jacobs, G.; Davis, B. H. Fischer−Tropsch: Product Selectivity−The Fingerprint of Synthetic Fuels. *Catalysts* **2019**, *9*, 259.

(9) Puga, A. v. On the Nature of Active Phases and Sites in CO and CO_2 Hydrogenation Catalysts. *Catal. Sci. Technol.* **2018**, *8*, 5681−5707.

(10) Khodakov, A. Y.; Chu, W.; Fongarland, P. Advances in the Development of Novel Cobalt Fischer-Tropsch Catalysts for Synthesis of Long-Chain Hydrocarbons and Clean Fuels. *Chem. Rev.* **2007**, *107*, 1692−1744.

(11) Paalanen, P. P.; Weckhuysen, B. M. Carbon Pathways, Sodium-Sulphur Promotion and Identification of Iron Carbides in Iron-Based Fischer-Tropsch Synthesis. *ChemCatChem* **2020**, *12*, 4202−4223.

(12) Gu, B.; Zhou, C.; He, S.; Moldovan, S.; Chernavskii, P. A.; Ordomsky, V. v.; Khodakov, A. Y. Size and Promoter Effects on Iron Nanoparticles Confined in Carbon Nanotubes and Their Catalytic Performance in Light Olefin Synthesis from Syngas. *Catal. Today* **2020**, *357*, 203−213.

(13) Cheng, Y.; Lin, J.; Xu, K.; Wang, H.; Yao, X.; Pei, Y.; Yan, S.; Qiao, M.; Zong, B. Fischer-Tropsch Synthesis to Lower Olefins over Potassium-Promoted Reduced Graphene Oxide Supported Iron Catalysts. *ACS Catal.* **2016**, *6*, 389−399.

(14) Nasser, A. L.-H.; El-Naggar, H.; El-Bery, H.; Basha, I.; Abdelmoneim, A. Correction: Utilizing FBR to Produce Olefins from CO Reduction Using Fe-Mn Nanoparticles on Reduced Graphene Oxide Catalysts and Comparing the Performance with SBR (RSC Adv. (2018) 8 (42415-42423) DOI: 10.1039/C8RA09003C). *RSC Adv.* **2019**, *9*, 10937.

(15) Dry, M. E. FT Catalysts. In *Studies in Surface Science and Catalysis*; Elsevier, 2004; Vol. *152*, pp 533−600.
(16) Nasser, A.-H.; Guo, L.; Elnaggar, H.; Wang, Y.; Guo, X.; Abdelmoneim, A.; Tsubaki, N. Mn-Fe Nanoparticles on a Reduced Graphene Oxide Catalyst for Enhanced Olefin Production from Syngas in a Slurry Reactor. *RSC Adv.* **2018**, *8*, 14854−14863.
(17) Nasser, A. H. M.; Elbery, H. M.; Anwar, H. N.; Basha, I. K.; Elnaggar, H. A.; Nakamura, K.; El-Moneim, A. A. A Study of Promoters Effect on Fe on Reduced Graphene Oxide Catalyst Performance in Fischer-Tropsch Synthesis System. *Key Eng. Mater.* **2017**, *735*, 143−147.
(18) Oschatz, M.; Krause, S.; Krans, N. A.; Hernández Mejía, C.; Kaskel, S.; de Jong, K. P. Influence of Precursor Porosity on Sodium and Sulfur Promoted Iron/Carbon Fischer-Tropsch Catalysts Derived from Metal-Organic Frameworks. *Chem. Commun.* **2017**, *53*, 10204−10207.
(19) Li, L.; Sun, L.; Cang, H.; Chu, W.; Shao, J.; Yan, J. Silica-Assisted Mesoporous Co@Carbon Nanoplates Derived from ZIF-67 Crystals and Their Enhanced Catalytic Activity. *J. Solid State Chem.* **2018**, *267*, 134−139.
(20) Tan, L.; Wang, F.; Zhang, P.; Suzuki, Y.; Wu, Y.; Chen, J.; Yang, G.; Tsubaki, N. Design of a Core-Shell Catalyst: An Effective Strategy for Suppressing Side Reactions in Syngas for Direct Selective Conversion to Light Olefins. *Chem. Sci.* **2020**, *11*, 4097−4105.
(21) Chen, Y.; Wei, J.; Duyar, M. S.; Ordomsky, V. v.; Khodakov, A. Y.; Liu, J. Carbon-Based Catalysts for Fischer-Tropsch Synthesis. *Chem. Soc. Rev.* **2021**, *50*, 2337−2366.
(22) Linares, N.; Silvestre-Albero, A. M.; Serrano, E.; Silvestre-Albero, J.; García-Martínez, J. Mesoporous Materials for Clean Energy Technologies. *Chem. Soc. Rev.* **2014**, *43*, 7681−7717.
(23) Rashed, A. E.; El-Moneim, A. A. Two Steps Synthesis Approach of MnO_2/Graphene Nanoplates/Graphite Composite Electrode for Supercapacitor Application. *Mater. Today Energy* **2017**, *3*, 24−31.
(24) Gamil, M.; Tabata, O.; Nakamura, K.; El-Bab, A. M. R. F.; El-Moneim, A. A. Investigation of a New High Sensitive Micro-Electromechanical Strain Gauge Sensor Based on Graphene Piezoresistivity. *Key Eng. Mater.* **2014**, *605*, 207−210.
(25) Gu, B.; Ordomsky, V. v.; Bahri, M.; Ersen, O.; Chernavskii, P. A.; Filimonov, D.; Khodakov, A. Y. Effects of the Promotion with Bismuth and Lead on Direct Synthesis of Light Olefins from Syngas over Carbon Nanotube Supported Iron Catalysts. *Appl. Catal., B* **2018**, *234*, 153−166.
(26) Wezendonk, T. A.; Sun, X.; Dugulan, A. I.; van Hoof, A. J. F.; Hensen, E. J. M.; Kapteijn, F.; Gascon, J. Controlled Formation of Iron Carbides and Their Performance in Fischer-Tropsch Synthesis. *J. Catal.* **2018**, *362*, 106−117.
(27) Cui, W.-G.; Zhang, G.-Y.; Hu, T.-L.; Bu, X.-H. Metal-Organic Framework-Based Heterogeneous Catalysts for the Conversion of C1 Chemistry: CO, CO_2 and CH_4. *Coord. Chem. Rev.* **2019**, *387*, 79−120.
(28) Luo, Q.-X.; Guo, L.-P.; Yao, S.-Y.; Bao, J.; Liu, Z.-T.; Liu, Z.-W. Cobalt Nanoparticles Confined in Carbon Matrix for Probing the Size Dependence in Fischer-Tropsch Synthesis. *J. Catal.* **2019**, *369*, 143−156.
(29) Oar-Arteta, L.; Wezendonk, T.; Sun, X.; Kapteijn, F.; Gascon, J. Metal Organic Frameworks as Precursors for the Manufacture of Advanced Catalytic Materials. *Mater. Chem. Front.* **2017**, *1*, 1709−1745.
(30) Qin, H.; Zhou, Y.; Huang, Q.; Yang, Z.; Dong, R.; Li, L.; Tang, J.; Zhang, C.; Jiang, F. Metal Organic Framework (MOF)/Wood Derived Multi-Cylinders High-Power 3D Reactor. *ACS Appl. Mater. Interfaces* **2021**, *13*, 5460−5468.
(31) Janani, H.; Rezvani, A.; Mirzaei, A. A. Preparation of a Novel Active Fischer−Tropsch Co−Ni Catalyst Derived from Metal-Organic Framework. *Pet. Chem.* **2020**, *60*, 1059−1065.
(32) Sun, B.; Tan, H.; Liu, S.; Lyu, S.; Zhang, X.; Zhang, Y.; Li, J.; Wang, L. Novel Cobalt Catalysts Supported on Metal−Organic Frameworks MIL-53(Al) for the Fischer−Tropsch Synthesis. *Energy Technol.* **2019**, *7*, 1800802.
(33) Santos, V. P.; Wezendonk, T. A.; Jaén, J. J. D.; Dugulan, A. I.; Nasalevich, M. A.; Islam, H.-U.; Chojecki, A.; Sartipi, S.; Sun, X.; Hakeem, A. A.; Koeken, A. C. J.; Ruitenbeek, M.; Davidian, T.; Meima, G. R.; Sankar, G.; Kapteijn, F.; Makkee, M.; Gascon, J. Metal Organic Framework-Mediated Synthesis of Highly Active and Stable Fischer-Tropsch Catalysts. *Nat. Commun.* **2015**, *6*, 6451.
(34) Wezendonk, T. A.; Santos, V. P.; Nasalevich, M. A.; Warringa, Q. S. E.; Dugulan, A. I.; Chojecki, A.; Koeken, A. C. J.; Ruitenbeek, M.; Meima, G.; Islam, H.-U.; Sankar, G.; Makkee, M.; Kapteijn, F.; Gascon, J. Elucidating the Nature of Fe Species during Pyrolysis of the Fe-BTC MOF into Highly Active and Stable Fischer-Tropsch Catalysts. *ACS Catal.* **2016**, *6*, 3236−3247.
(35) Wezendonk, T. A.; Warringa, Q. S. E.; Santos, V. P.; Chojecki, A.; Ruitenbeek, M.; Meima, G.; Makkee, M.; Kapteijn, F.; Gascon, J. Structural and Elemental Influence from Various MOFs on the Performance of Fe@C Catalysts for Fischer-Tropsch Synthesis. *Faraday Discuss.* **2017**, *197*, 225−242.
(36) An, B.; Cheng, K.; Wang, C.; Wang, Y.; Lin, W. Pyrolysis of Metal-Organic Frameworks to Fe_3O_4@Fe_5C_2 Core-Shell Nanoparticles for Fischer-Tropsch Synthesis. *ACS Catal.* **2016**, *6*, 3610−3618.
(37) Yang, X.; Guo, X.; Zhang, C.; Wang, X.; Yang, Y.; Li, Y. Synthesis and Catalytic Properties of Iron Based Fischer-Tropsch Catalyst Mediated by MOFs Fe-MIL-100. *Acta Phys. Chim. Sin.* **2017**, *75*, 360−366.
(38) Oar-Arteta, L.; Valero-Romero, M. J.; Wezendonk, T.; Kapteijn, F.; Gascon, J. Formulation and Catalytic Performance of MOF-Derived Fe@C/Al Composites for High Temperature Fischer-Tropsch Synthesis. *Catal. Sci. Technol.* **2018**, *8*, 210−220.
(39) Zhao, Q.; Huang, S.; Han, X.; Chen, J.; Wang, J.; Rykov, A.; Wang, Y.; Wang, M.; Lv, J.; Ma, X. Highly Active and Controllable MOF-Derived Carbon Nanosheets Supported Iron Catalysts for Fischer-Tropsch Synthesis. *Carbon* **2021**, *173*, 364−375.
(40) Wu, Y.; Huang, Z.; Jiang, H.; Wang, C.; Zhou, Y.; Shen, W.; Xu, H.; Deng, H. Facile Synthesis of Uniform Metal Carbide Nanoparticles from Metal−Organic Frameworks by Laser Metallurgy. *ACS Appl. Mater. Interfaces* **2019**, *11*, 44573−44581.
(41) Cheng, K.; Virginie, M.; Ordomsky, V. v.; Cordier, C.; Chernavskii, P. A.; Ivantsov, M. I.; Paul, S.; Wang, Y.; Khodakov, A. Y. Pore Size Effects in Higherature Fischer-Tropsch Synthesis over Supported Iron Catalysts. *J. Catal.* **2015**, *328*, 139−150.
(42) Ma, W.; Dalai, A. K. Effects of Structure and Particle Size of Iron, Cobalt and Ruthenium Catalysts on Fischer−Tropsch Synthesis. *Reactions* **2021**, *2*, 62−77.
(43) Wei, Y.; Yan, L.; Ma, C.; Zhang, C.; Sun, S.; Wen, X.; Yang, Y.; Li, Y. Mesoporous Iron Oxide Nanoparticle-Decorated Graphene Oxide Catalysts for Fischer-Tropsch Synthesis. *ACS Appl. Nano Mater.* **2020**, *3*, 7182−7191.
(44) Chen, W.; Lin, T.; Dai, Y.; An, Y.; Yu, F.; Zhong, L.; Li, S.; Sun, Y. Recent Advances in the Investigation of Nanoeffects of Fischer-Tropsch Catalysts. *Catal. Today* **2018**, *311*, 8−22.
(45) Iglesia, E. Design, Synthesis, and Use of Cobalt-Based Fischer-Tropsch Synthesis Catalysts. *Appl. Catal., A* **1997**, *161*, 59−78.
(46) Bezemer, G. L.; Bitter, J. H.; Kuipers, H. P. C. E.; Oosterbeek, H.; Holewijn, J. E.; Xu, X.; Kapteijn, F.; van Dillen, A. J.; de Jong, K. P. Cobalt Particle Size Effects in the Fischer-Tropsch Reaction Studied with Carbon Nanofiber Supported Catalysts. *J. Am. Chem. Soc.* **2006**, *128*, 3956−3964.
(47) Jung, H.; Walker, P. L.; Vannice, A. CO Hydrogenation over Well-Dispersed Carbon-Supported Iron Catalysts. *J. Catal.* **1982**, *75*, 416−422.
(48) Jones, V. K.; Neubauer, L. R.; Bartholomew, C. H. Effects of Crystallite Size and Support on the CO Hydrogenation Activity/Selectivity Properties of Fe/Carbon. *J. Phys. Chem.* **1986**, *90*, 4832−4839.
(49) Barkhuizen, D.; Mabaso, I.; Viljoen, E.; Welker, C.; Claeys, M.; van Steen, E.; Fletcher, J. C. Q. Experimental Approaches to the Preparation of Supported Metal Nanoparticles. *Pure Appl. Chem.* **2006**, *78*, 1759−1769.

https://doi.org/10.1021/acsomega.1c05927
ACS Omega 2022, 7, 8403−8419

(50) Mabaso, E. I.; van Steen, E.; Claeys, M. *Fischer-Tropsch Synthesis on Supported Iron Crystallites of Different Size*; DGMK Tagungsbericht, 2006; pp 93−100.
(51) Park, J.-Y.; Lee, Y. J.; Khanna, P. K.; Jun, K. W.; Bae, J. W.; Kim, Y. H. Alumina-Supported Iron Oxide Nanoparticles as Fischer-Tropsch Catalysts: Effect of Particle Size of Iron Oxide. *J. Mol. Catal. A: Chem.* **2010**, *323*, 84−90.
(52) Torres Galvis, H. M.; Bitter, J. H.; Davidian, T.; Ruitenbeek, M.; Dugulan, A. I.; de Jong, K. P. Iron Particle Size Effects for Direct Production of Lower Olefins from Synthesis Gas. *J. Am. Chem. Soc.* **2012**, *134*, 16207−16215.
(53) Xie, J.; Torres Galvis, H. M.; Koeken, A. C. J.; Kirilin, A.; Dugulan, A. I.; Ruitenbeek, M.; de Jong, K. P. Size and Promoter Effects on Stability of Carbon-Nanofiber-Supported Iron-Based Fischer-Tropsch Catalysts. *ACS Catal.* **2016**, *6*, 4017−4024.
(54) Xie, J.; Yang, J.; Dugulan, A. I.; Holmen, A.; Chen, D.; de Jong, K. P.; Louwerse, M. J. Size and Promoter Effects in Supported Iron Fischer-Tropsch Catalysts: Insights from Experiment and Theory. *ACS Catal.* **2016**, *6*, 3147−3157.
(55) Liu, Y.; Chen, J.-F.; Zhang, Y. The Effect of Pore Size or Iron Particle Size on the Formation of Light Olefins in Fischer-Tropsch Synthesis. *RSC Adv.* **2015**, *5*, 29002−29007.
(56) Sun, Z.; Sun, B.; Qiao, M.; Wei, J.; Yue, Q.; Wang, C.; Deng, Y.; Kaliaguine, S.; Zhao, D. A General Chelate-Assisted Co-Assembly to Metallic Nanoparticles- Incorporated Ordered Mesoporous Carbon Catalysts for Fischer-Tropsch Synthesis. *J. Am. Chem. Soc.* **2012**, *134*, 17653−17660.
(57) Iablokov, V.; Xiang, Y.; Meffre, A.; Fazzini, P.-F.; Chaudret, B.; Kruse, N. Size-Dependent Activity and Selectivity of Fe/MCF-17 in the Catalytic Hydrogenation of Carbon Monoxide Using Fe(0) Nanoparticles as Precursors. *ACS Catal.* **2016**, *6*, 2496−2500.
(58) Liu, J.-X.; Wang, P.; Xu, W.; Hensen, E. J. M. Particle Size and Crystal Phase Effects in Fischer-Tropsch Catalysts. *Engineering* **2017**, *3*, 467−476.
(59) Zhao, X.; Lv, S.; Wang, L.; Li, L.; Wang, G.; Zhang, Y.; Li, J. Comparison of Preparation Methods of Iron-Based Catalysts for Enhancing Fischer-Tropsch Synthesis Performance. *J. Mol. Catal.* **2018**, *449*, 99−105.
(60) Bauer, S.; Serre, C.; Devic, T.; Horcajada, P.; Marrot, J.; Férey, G.; Stock, N. High-Throughput Assisted Rationalization of the Formation Iron (III) Aminoterephthalate Solvothermal System. *Inorg. Chem.* **2008**, *47*, 7568−7576.
(61) Sánchez-Sánchez, M.; Getachew, N.; Díaz, K.; Díaz-García, M.; Chebude, Y.; Díaz, I. Synthesis of Metal-Organic Frameworks in Water at Room Temperature: Salts as Linker Sources. *Green Chem.* **2015**, *17*, 1500−1509.
(62) Lu, H.; Zhu, S. Interfacial Synthesis of Free-Standing Metal-Organic Framework Membranes. *Eur. J. Inorg. Chem.* **2013**, 1294−1300.
(63) Horcajada, P.; Salles, F.; Wuttke, S.; Devic, T.; Heurtaux, D.; Maurin, G.; Vimont, A.; Daturi, M.; David, O.; Magnier, E.; Stock, N.; Filinchuk, Y.; Popov, D.; Riekel, C.; Férey, G.; Serre, C. How Linker's Modification Controls Swelling Properties of Highly Flexible Iron(III) Dicarboxylates MIL-88. *J. Am. Chem. Soc.* **2011**, *133*, 17839−17847.
(64) Rashed, A. E.; Essam, K.; El-Kady, M. F.; Yoshihisa, M.; El-Moneim, A. A.; Nasser, A. Highly Active Fischer-Tropsch Synthesis Fe-BDC MOF-Derived Catalyst Prepared by Modified Solvothermal Method. *Key Eng. Mater.* **2021**, *891*, 56−61.
(65) El-Khatib, K. M.; Abou Helal, M. O.; El-Moneim, A. A.; Tawfik, H. Corrosion Stability of SUS316L HVOF Sprayed Coatings as Lightweight Bipolar Plate Materials in PEM Fuel Cells. *Anti-Corros. Methods Mater.* **2004**, *51*, 136−142.
(66) El-Moneim, A. A.; Akiyama, E.; Ismail, K. M.; Hashimoto, K. Corrosion Behaviour of Sputter-Deposited Mg−Zr Alloys in a Borate Buffer Solution. *Corros. Sci.* **2011**, *53*, 2988−2993.
(67) Lou, X.; Hu, H.; Li, C.; Hu, X.; Li, T.; Shen, M.; Chen, Q.; Hu, B. Capacity Control of Ferric Coordination Polymers by Zinc Nitrate for Lithium-Ion Batteries. *RSC Adv.* **2016**, *6*, 86126−86130.
(68) Nguyen, V.; Nguyen, T. D.; Bach, L. G.; Hoang, T.; Bui, Q. T. P.; Tran, L. D.; Nguyen, C. v.; Vo, D. V. N.; Do, S. T. Effective Photocatalytic Activity of Mixed Ni/Fe-Base Metal-Organic Framework under a Compact Fluorescent Daylight Lamp. *Catalysts* **2018**, *8*, 487.
(69) Chirita, M.; Banica, R.; Ieta, A.; Grozescu, I. Superparamagnetic Unusual Behavior of Micrometric Magnetite Monodisperse Monocrystals Synthesized by Fe-EDTA Thermal Decomposition. *Part. Sci. Technol.* **2012**, *30*, 354−363.
(70) Ahmadpoor, F.; Shojaosadati, S. A.; Delavari, H. H.; Christiansen, G.; Saber, R. Synthesis of Fe_5C_2@SiO_2 Core@shell Nanoparticles as a Potential Candidate for Biomedical Application. *Mater. Res. Express* **2018**, *5*, 055038.
(71) Ebrahiminezhad, A.; Ghasemi, Y.; Rasoul-Amini, S.; Barar, J.; Davaran, S. Impact of Amino-Acid Coating on the Synthesis and Characteristics of Iron-Oxide Nanoparticles (IONs). *Bull. Korean Chem. Soc.* **2012**, *33*, 3957−3962.
(72) Pu, M.; Guan, Z.; Ma, Y.; Wan, J.; Wang, Y.; Brusseau, M. L.; Chi, H. Synthesis of Iron-Based Metal-Organic Framework MIL-53 as an Efficient Catalyst to Activate Persulfate for the Degradation of Orange G in Aqueous Solution. *Appl. Catal., A* **2018**, *549*, 82−92.
(73) Gorimbo, J.; Muleja, A.; Liu, X.; Hildebrandt, D. Fischer−Tropsch Synthesis: Product Distribution, Operating Conditions, Iron Catalyst Deactivation and Catalyst Speciation. *Int. J. Ind. Chem.* **2018**, *9*, 317−333.
(74) de Smit, E.; Weckhuysen, B. M. The Renaissance of Iron-Based Fischer-Tropsch Synthesis: On the Multifaceted Catalyst Deactivation Behaviour. *Chem. Soc. Rev.* **2008**, *37*, 2758−2781.
(75) Chen, W.; Kimpel, T. F.; Song, Y.; Chiang, F.-K.; Zijlstra, B.; Pestman, R.; Wang, P.; Hensen, E. J. M. Influence of Carbon Deposits on the Cobalt-Catalyzed Fischer-Tropsch Reaction: Evidence of a Two-Site Reaction Model. *ACS Catal.* **2018**, *8*, 1580−1590.
(76) Ni, Z.; Qin, H.; Kang, S.; Bai, J.; Wang, Z.; Li, Y.; Zheng, Z.; Li, X. Effect of Graphitic Carbon Modification on the Catalytic Performance of Fe@SiO_2-GC Catalysts for Forming Lower Olefins via Fischer-Tropsch Synthesis. *J. Colloid Interface Sci.* **2018**, *516*, 16−22.
(77) Fang, Q.-R.; Makal, T. A.; Young, M. D.; Zhou, H. C. Recent Advances in the Study of Mesoporous Metal-Organic Frameworks. *Comments Inorg. Chem.* **2010**, *31*, 165−195.
(78) Donohue, M. D.; Aranovich, G. L. Adsorption Hysteresis in Porous Solids. *J. Colloid Interface Sci.* **1998**, *205*, 121−130.
(79) Yang, J.; Ma, W.; Chen, D.; Holmen, A.; Davis, B. H. Fischer-Tropsch Synthesis: A Review of the Effect of CO Conversion on Methane Selectivity. *Appl. Catal., A* **2014**, *470*, 250−260.
(80) Su, J.; Zhou, H.; Liu, S.; Wang, C.; Jiao, W.; Wang, Y.; Liu, C.; Ye, Y.; Zhang, L.; Zhao, Y.; Liu, H.; Wang, D.; Yang, W.; Xie, Z.; He, M. Syngas to Light Olefins Conversion with High Olefin/Paraffin Ratio Using $ZnCrO_x$/AlPO-18 Bifunctional Catalysts. *Nat. Commun.* **2019**, *10*, 1297.
(81) Tu, J.; Yuan, J.; Kang, S.; Xu, Y.; Wang, T. One-Pot Synthesis of Carbon-Coated Fe_3O_4 Nanoparticles with Tunable Size for Production of Gasoline Fuels. *New J. Chem.* **2018**, *42*, 10861−10867.
(82) Housaindokht, M. R.; Nakhaei Pour, A. Size Control of Iron Oxide Nanoparticles Using Reverse Microemulsion Method: Morphology, Reduction, and Catalytic Activity in CO Hydrogenation. *J. Chem.* **2013**, *2013*, 1.
(83) Liu, L.; Corma, A. Metal Catalysts for Heterogeneous Catalysis: From Single Atoms to Nanoclusters and Nanoparticles. *Chem. Rev.* **2018**, *118*, 4981−5079.
(84) Campbell, C. T. The Energetics of Supported Metal Nanoparticles: Relationships to Sintering Rates and Catalytic Activity. *Acc. Chem. Res.* **2013**, *46*, 1712−1719.
(85) Mehar U Nisa, U. N.; Chen, Y.; Li, X.; Li, Z. Highly Efficient Iron Based MOFs Mediated Catalysts for Fischer−Tropsch Synthesis: Effect of Reduction Atmosphere. *J. Taiwan Inst. Chem. Eng.* **2020**, *107*, 44−53.

https://doi.org/10.1021/acsomega.1c05927
ACS Omega 2022, 7, 8403−8419